

**DOT/FAA/AR-08/36**

Air Traffic Organization  
Operations Planning  
Office of Aviation Research  
and Development  
Washington, DC 20591

# **Explicit Finite Element Analysis of 2024-T3/T351 Aluminum Material Under Impact Loading for Airplane Engine Containment and Fragment Shielding**

September 2008

Final Report

This document is available to the U.S. public  
through the National Technical Information  
Service (NTIS), Springfield, Virginia 22161.



U.S. Department of Transportation  
**Federal Aviation Administration**

## **NOTICE**

This document is disseminated under the sponsorship of the U.S. Department of Transportation in the interest of information exchange. The United States Government assumes no liability for the contents or use thereof. The United States Government does not endorse products or manufacturers. Trade or manufacturer's names appear herein solely because they are considered essential to the objective of this report. This document does not constitute FAA certification policy. Consult your local FAA aircraft certification office as to its use.

This report is available at the Federal Aviation Administration William J. Hughes Technical Center's Full-Text Technical Reports page: [actlibrary.tc.faa.gov](http://actlibrary.tc.faa.gov) in Adobe Acrobat portable document format (PDF).

1. Report No. DOT/FAA/AR-08/36		2. Government Accession No.		3. Recipient's Catalog No.	
4. Title and Subtitle  EXPLICIT FINITE ELEMENT ANALYSIS OF 2024-T3/T351 ALUMINUM MATERIAL UNDER IMPACT LOADING FOR AIRPLANE ENGINE CONTAINMENT AND FRAGMENT SHIELDING				5. Report Date  September 2008	
				6. Performing Organization Code	
7. Author(s) Murat Buyuk**, Matti Loikkanen*, and Cing-Dao (Steve) Kan**				8. Performing Organization Report No.	
9. Performing Organization Name and Address  **The George Washington University FHWA/NHTSA National Crash Analysis Center 20101 Academic Way Ashburn, VA 20147 USA  *The Boeing Company Commercial Airplanes PO Box 3707 Seattle, WA 98124-2207				10. Work Unit No. (TRAIS)	
				11. Contract or Grant No.	
12. Sponsoring Agency Name and Address  U.S. Department of Transportation Federal Aviation Administration Air Traffic Organization Operations Planning Office of Aviation Research and Development Washington, DC 20591				13. Type of Report and Period Covered  Final Report	
				14. Sponsoring Agency Code ANM-100/AME-100	
15. Supplementary Notes The Federal Aviation Administration Airport and Aircraft Safety R&D Division COTR was Donald Altobelli.					
16. Abstract Uncontained aircraft engine failure can cause catastrophic damaging effects to aircraft systems if not addressed in the aircraft design. The Federal Aviation Administration has commissioned and coordinated a research program associating industry, government agencies, national research laboratories, and universities to conduct research to mitigate the damaging effects of uncontained engine failure and improve the numerical modeling capability of these uncontained engine events. This joint Boeing and George Washington University report covers high strain rate material modeling efforts that have been conducted to simulate and validate ballistic impact tests on 2024-T3/T351 aluminum alloy, which is one of the most extensively used materials in the aircraft industry.  Ballistic limits were evaluated using explicit finite element (FE) simulations based on the corresponding ballistic impact experiments for different target thicknesses that were conducted at the University of California at Berkeley. LS-DYNA <sup>®</sup> was used as a nonlinear explicit dynamics FE code for the simulations. The Johnson-Cook material model was employed as a thermo-visco-plastic material model coupled with a nonlinear equation of state and an accumulated damage evaluation algorithm for the numerical simulations. Predictive performance of the numerical models is discussed in terms of the material characterization efforts and material model parameter sensitivities.					
17. Key Words  Uncontained engine failure, Impact, Aircraft engine fragments, Containment, Finite element analysis, High strain rate			18. Distribution Statement  This document is available to the U.S. public through the National Technical Information Service (NTIS), Springfield, Virginia 22161.		
19. Security Classif. (of this report) Unclassified		20. Security Classif. (of this page) Unclassified		21. No. of Pages 48	
22. Price					

## TABLE OF CONTENTS

	Page
EXECUTIVE SUMMARY	x
1. INTRODUCTION	1
1.1 Purpose	2
1.2 Background	2
2. BALLISTIC IMPACT TEST RESULTS	3
3. NUMERICAL MODELING	4
3.1 Finite Element Models	4
3.1.1 Models With Spherical Projectile for Through-the-Thickness Mesh Dependency	4
3.1.2 Model With Spherical Projectile for Mesh Pattern Dependency	6
3.1.3 Model With Cylindrical Projectile	7
3.1.4 Model With Prismatic Projectile	8
3.2 Material Model	8
3.2.1 The J-C Material Model	9
3.2.2 Mie-Gruneisen EOS	10
3.2.3 Material Characterization	10
3.3 Bulk Viscosity	13
3.4 Contact Definitions	13
3.5 Nonlocal Failure	14
3.6 Computing Platforms	14
4. BALLISTIC IMPACT SIMULATION RESULTS FOR DIFFERENT MESHES	14
4.1 Target Thickness 1/16"	15
4.2 Target Thickness 1/8"	18
4.3 Target Thickness 1/4"	21
5. THE EFFECTS OF MATERIAL MODEL PARAMETERS	24
5.1 Platform Dependency and Computational Cost	29

5.2	Ballistic Limit Summary and Discussion	32
6.	COMPARING AND DISCUSSING THE PENETRATION EQUATIONS	33
7.	CONCLUSIONS	36
8.	REFERENCES	36

## LIST OF FIGURES

Figure		Page
1	Experimental Ballistic Limit Evaluation for 2024-T3/T351 at Different Target Material Thicknesses	3
2	Quarter Symmetric Ballistic Impact Model	4
3	Close-Up of the Mesh-I, Coarse Mesh, 1/16" Target Model	5
4	Close-Up of the Mesh-II, Fine Mesh, 1/16" Target Model	6
5	Close-Up of the Mesh-I, Coarse Mesh, 1/4" Target Model	6
6	Close-Up of the Mesh-III, 1/16" Target Model	7
7	A 1/4" Target With Cylindrical Projectile, Mesh-I	8
8	A 1/4" Target With Prismatic Projectile, Mesh-I	8
9	Differences in the Yield Surface Data for 2024-T3/T351	12
10	Differences in the Fracture Locus Data for 2024-T3/T351	12
11	Determination of the Characteristic Length for Nonlocal Failure Option	14
12	Penetration Through 1/16" Target and Petal Formation	15
13	Ballistic Limit Predictions for LLNL-2 Material Data, 1/16" Target	16
14	Ballistic Limit Predictions for LLNL-3 Material Data, 1/16" Target	16
15	Ballistic Limit Predictions for LLNL-3 Material Data With Segment Contact, 1/16" Target	17
16	Ballistic Limit Predictions for LLNL-3 Material Data With Nonlocal Smoothing, 1/16" Target	17
17	Penetration Through 1/8" Target and Mixed Mode Failure	18
18	Ballistic Limit Predictions for LLNL-2 Material Data, 1/8" Target	19
19	Ballistic Limit Predictions for LLNL-3 Material Data, 1/8" Target	19

20	Ballistic Limit Predictions for LLNL-3 Material Data With Segment Contact, 1/8" Target	20
21	Ballistic Limit Predictions for LLNL-3 Material Data With Nonlocal Smoothing, 1/8" Target	20
22	Penetration Through 1/4" Target and Plugging	21
23	Ballistic Limit Predictions for LLNL-2 Material Data, 1/4" Target	22
24	Ballistic Limit Predictions for LLNL-3 Material Data, 1/4" Target	22
25	Ballistic Limit Predictions for LLNL-3 Material Data With Segment Contact, 1/4" Target	23
26	Ballistic Limit Prediction for LLNL-3 Material Data With Nonlocal Smoothing, 1/4" Target	23
27	Ballistic Impact Simulation for 1/16" 2024-T3 Target	24
28	Ballistic Impact Test Results for 1/16" 2024-T3 Target (a) Front and (b) Rear View	25
29	Ballistic Limit Predictions (Mesh-III) for 1/16" 2024-T3	25
30	Ballistic Impact Simulation for 1/8" 2024-T3 Target	26
31	Ballistic Impact Test Result for 1/8" 2024-T3 Target (a) Front and (b) Rear View	26
32	Ballistic Limit Predictions (Mesh-III) for 1/8" 2024-T3	27
33	Ballistic Impact Simulation for 1/4" 2024-T351 Target	28
34	Ballistic Impact Test Results for 1/4" 2024-T351 Target (a) Front and (b) Rear View	28
35	Ballistic Limit Predictions (Mesh-III) for 1/4" 2024-T351	29
36	Platform Dependency for Target Thickness 1/16"	30
37	Platform Dependency for Target Thickness 1/8"	30
38	Platform Dependency for Target Thickness 1/4"	31
39	Cross-Platform Comparison of the Normalized Computing Costs	31
40	Transition of the Failure Mode	32

41	Ballistic Limit Comparison for Spherical, Cubical, and Cylindrical Projectiles for 1/16" Target	33
42	Ballistic Limit Comparison for Spherical, Cubical, and Cylindrical Projectiles for 1/8" Target	34
43	Ballistic Limit Comparison for Spherical, Cubical, and Cylindrical Projectiles for 1/4" Target	34
44	Comparison of the Ballistic Limit Predictions	35



## LIST OF TABLES

Table		Page
1	The FE Models and Corresponding Model Sizes	7
2	The J-C Material Model Parameters	11
3	Bulk Viscosity Coefficients	13

## LIST OF ACRONYMS

3D	Three-dimensional
EOS	Equation of state
FAA	Federal Aviation Administration
FE	Finite element
GWU	George Washington University
J-C	Johnson-Cook
LLNL	Lawrence Livermore National Laboratory
LSTC	Livermore Software Technology Corporation
SHPB	Split Hopkinson Pressure Bar
SGI	Silicon Graphics, Inc.
UCB	University of California at Berkeley
V <sub>50</sub>	Ballistic limit

## EXECUTIVE SUMMARY

Uncontained aircraft engine failure can cause catastrophic damaging effects to aircraft systems if not addressed in the aircraft design. The Federal Aviation Administration has commissioned and coordinated a research program associating industry, government agencies, national research laboratories, and universities to conduct research to mitigate the damaging effects of uncontained engine failure and improve the numerical modeling capability of these uncontained engine events. This joint Boeing Company and George Washington University report covers high strain rate material modeling efforts that have been conducted to simulate and validate ballistic impact tests on 2024-T3/T351 aluminum alloy, which is one of the most extensively used materials in the aircraft industry.

Ballistic limits were evaluated by using explicit finite element (FE) simulations based on the corresponding ballistic impact experiments for different 2024-T3 aluminum target thicknesses, which were conducted at the University of California at Berkeley. LS-DYNA<sup>®</sup> was used as a nonlinear explicit dynamics FE code for the simulations. Johnson-Cook (J-C) material model was employed as a thermo-visco-plastic material model coupled with a nonlinear equation of state and an accumulated damage evaluation algorithm for the numerical simulations. Predictive performance of the numerical models is discussed in terms of the material characterization efforts and material model parameter sensitivities.

It was shown that the characterization for a specific type of material at a particular thickness and at a particular strain rate may not necessarily be enough to simulate the overall ballistic impact performance of this material. Changes in thickness and impact velocity can lead to a change in the deformation mechanism and response of the material. The J-C material model may exhibit some limitations while simulating these transitions. It was concluded that new constitutive models, which can cover a wider range of material response, should be developed to simulate the material behavior more accurately under ballistic impact loading.

## 1. INTRODUCTION.

High strain rate material characterization was investigated under the Federal Aviation Administration (FAA) Aircraft Catastrophic Failure Prevention Program as part of the research of uncontained engine failure events. The Boeing Company teamed with the University of California at Berkeley (UCB) and the Lawrence Livermore National Laboratory (LLNL) at Livermore, CA, to develop technologies to assist in the design of fragment barriers to mitigate the impact from jet engine debris in the case of rotor failure. This phase of the study focused on improving the understanding of metal fragments impacting and penetrating aluminum airframe parts, such as wings and fuselage, that are in close proximity to the engines. This effort consisted of testing 2024 aluminum alloy for high strain rate material properties, ballistic impact testing, development of finite element (FE) modeling techniques, and simulation of the test results. Material characterization of 2024-T3/T351 aluminum for deformation and failure behavior were attained by the LLNL. Characterization data was obtained at high strain rates and large strains using the Split Hopkinson Pressure Bar (SHPB) method. A new set of material constants for the strength component of the Johnson-Cook (J-C) material model for 2024-T3/T351 was found and compared to the existing data from the literature [1-4].

Ballistic impact tests were conducted by LLNL [4] and UCB [5]. LLNL performed additional simulations [3] using the recent test data that included thicker targets than the previous data [2]. Corresponding numerical simulations were also performed by Boeing. Boeing's effort focused on the development of FE analysis methods and simulation of the test results. FE models were built and exercised in the simulation runs. The computational and experimental results were compared with the tests, and the models were fine-tuned as needed. The George Washington University (GWU) became a part of this study through an Airworthiness Assurance Center of Excellence grant to conduct modeling efforts for the ballistic impact simulations. Within this research task, GWU supported Boeing and teamed with Livermore Software Technology Corporation (LSTC) and Silicon Graphics, Inc. (SGI) to simulate and validate ballistic impact tests by using different sets of J-C material model parameters that were characterized and extracted by LLNL. This report summarizes the results of the Boeing and GWU work on aluminum material simulations.

Reliable ballistic impact computations are still a challenge. Advanced computer codes are available and many material models exist to depict the behavior of metals under high-speed impact. However, the material data is often not publicly available or may not comprise the needed high strain rate behavior regime that is required for these ballistic impact studies. Also, critical details of the numerical modeling methodologies are usually not very well defined.

In this research, newly refined J-C material data for 2024-T3/T351 aluminum was used and some joint modeling efforts of GWU and Boeing are addressed and described. Different numerical options, such as meshing, contact definitions, damping and nonlocal smoothing were investigated to delineate their effects on the ballistic limit predictions. UCB ballistic impact tests were used to compare the simulation results.

## 1.1 PURPOSE.

The overall purpose of this research and joint objective of GWU and Boeing was to develop practical FE modeling guidelines for the aviation community to predict ballistic impact performance of aeronautical structures with reasonable accuracy and computational cost. Since the predictive capability of the numerical models is directly related to the competence of the employed constitutive law and material model, the performance of one of the very widely used material models was investigated with the available experimental data. The results of this study will be used to help define the material and failure models of the LS-DYNA<sup>®</sup> nonlinear FE code.

## 1.2 BACKGROUND.

The deformation and failure behavior of Ti-6Al-4V titanium and 2024-T3/T351 aluminum was studied by LLNL under an Interagency Agreement between the FAA William J. Hughes Technical Center and the Department of Energy within the FAA's Aircraft Catastrophic Failure Prevention Program, as part of its research into the turbine engine uncontainment event [2].

The material characterization gathered by LLNL through the SHPB test method and additional data from the literature were used to evaluate the ability of the J-C material model to represent the deformation and failure response of Ti-6Al-4V and 2024-T3/T351 under conditions relevant to simulations of engine containment and the influence of uncontained engine debris on aircraft structures. The original J-C parameters are referred to as "Literature" in this report. LLNL material characterization test results were used to evaluate the ability of the J-C material model to represent the deformation and failure response of Ti-6Al-4V and 2024-T3/T351 under conditions relevant to simulations of engine containment and the influence of uncontained engine debris on aircraft structures. This first set of J-C parameters for 2024 T3/351 aluminum [2] is referred to as "LLNL-1" in this report.

To get more representative data for aircraft skin, LLNL conducted a series of ballistic impact tests, which were used to further refine the J-C parameters [6]. Using this test data, LLNL developed a new set of J-C parameters for Ti-6Al-4V titanium and 2024-T3/T351 aluminum [3]. This second set of parameters for 2024 T3/T351 aluminum is referred to as "LLNL-2" in this report.

In a recent study, LLNL recalibrated the J-C failure parameters for 2024 T3/T351 aluminum to attain consistency between simulations and the available ballistic limit measurements [4]. Ballistic impact test data used for this recalibration were conducted by UCB [5] and consisted of thicker aluminum targets than previously tested. Gas and powder gun tests were performed to determine the ballistic speed limit of a spherical steel projectile with a diameter of 1/2". The rectangular flat aluminum targets were prepared as 12" by 12" targets with three different thickness combinations of 1/16", 1/8", and 1/4". Spherical projectiles were used to better simulate a normal impact scenario in terms of the orientation of the specimens to the impacting projectile. It was shown that the aluminum plates failed by dishing and petaling with slight plugging for the thinnest targets. As the thickness increased, the amount of dishing and petaling decreased and the failure mode tended towards plugging. The ballistic tests confirmed the transition of the failure mode with the change in thickness and corresponding increase in speed.

This third set of parameters for 2024 T3/T351 aluminum is referred to as “LLNL-3” in this report.

In a successive study that was conducted by GWU and Boeing, UCB tests were also modeled and simulated by using three-dimensional (3D) FE models, while three sets of material model parameters were evaluated according to their predictive performance for the ballistic limits [7]. It was shown that different sets of parameters have different levels of success in predicting the ballistic limit depending on the change in the thickness of the target material.

## 2. BALLISTIC IMPACT TEST RESULTS.

Figure 1 summarizes the ballistic test results that were conducted at UCB [5]. The tests with initial velocities below 1000 ft/s were performed with a pneumatic gun; a powder gun was used for higher impact velocities. The target plate thicknesses were 1/16", 1/8", and 1/4". The plates were cut to a 12" by 12" size and attached to the 1" wide support frame, leaving a 10" by 10" free target area. The projectile was a 1/2" diameter 52100 chrome alloy steel sphere.

Ductile materials, such as aluminum, exhibited a sharp rise in the exit velocity plot just after the ballistic limit [8]. As shown in figure 1, after the ballistic limit, the residual velocity rose sharply and later followed a 45-degree slope, which is a characteristic property for many ductile materials. From these test results with the spherical projectile, the ballistic limit for 1/16" plate was found to be about 400 ft/s, for 1/8" thickness it was about 700 ft/s, and for 1/4" thickness it was about 1350 ft/s.

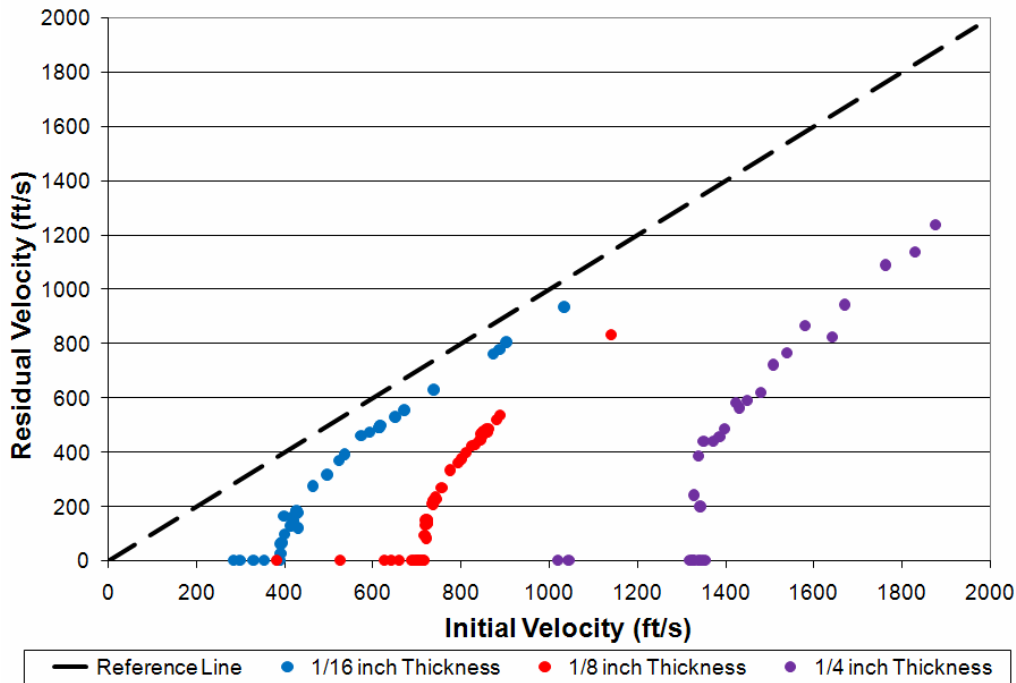


Figure 1. Experimental Ballistic Limit Evaluation for 2024-T3/T351 at Different Target Material Thicknesses

### 3. NUMERICAL MODELING.

All numerical models in this study were developed to be used with LS-DYNA as a nonlinear explicit dynamics FE numerical solver.

#### 3.1 FINITE ELEMENT MODELS.

Sections 3.1.1, 3.1.3, and 3.1.4 discuss quarter symmetric FE models developed by Boeing to investigate their predictive performance, while several different modeling parameters, such as bulk viscosity, contact options, and nonlocal smoothing, were examined. These models are cost-effective 3D models, where a nearly perfect hit with nonoblique projectile orientation can be modeled successfully. Since the target and the projectile were symmetrical about both the horizontal and vertical axes, only one quarter model of the test target and the projectile was developed.

Section 3.1.2 discusses another quarter symmetric model developed by GWU with predetermined modeling parameters. The mesh pattern dependency was examined to find an optimized mesh for stability, accuracy, and efficiency of the impact analysis. The predictive performance of the four available sets of material model parameters for aluminum was investigated and the results were compared with the UCB test data. The latter model was created also to investigate platform dependency in terms of accuracy and computational cost.

##### 3.1.1 Models With Spherical Projectile for Through-the-Thickness Mesh Dependency.

Both the target and projectile are modeled with 8-node hexagonal solid elements. A typical model with 1/4" thickness is shown in figure 2. The FE model took advantage of the double symmetry through the center. One quarter of the target and the projectile were in the positive x-y quadrant with the center at the origin. Fully fixed boundary conditions were imposed on the outer boundary and the symmetry boundary conditions were imposed at  $x=0.0$  and  $y=0.0$  simulating the target translations and rotations. The rotation about the x-axis (at  $y=0$ ) was constrained by fixing the y-translation on that surface of the model. The projectile y-translations were fixed at  $y=0$  and x-translations were fixed at  $x=0$  in the model.

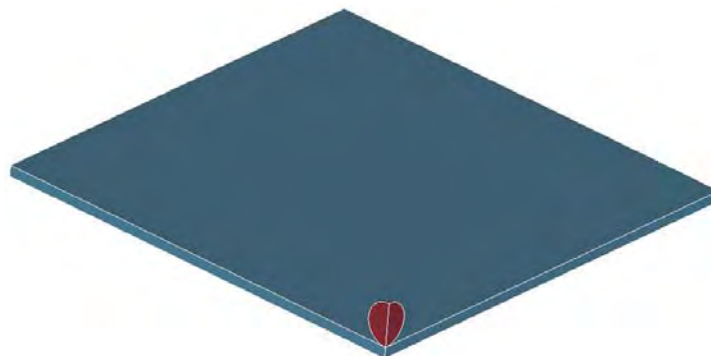


Figure 2. Quarter Symmetric Ballistic Impact Model

The mesh pattern in the x-y plane is shown in figure 3. The mesh just under the projectile was chosen to be circular to assure that the failure would occur along the element boundaries. The mesh density under the impact zone was also finer than the surrounding. The in-plane mesh pattern was kept the same for all models, while the element size through-the-thickness (z-direction) was varied. Each target thickness was modeled with two mesh densities, while many more were investigated during the trial runs. As a characteristic of the nonlinear FE analysis, simply refining the mesh does not necessarily improve the solution accuracy as is usually the case for quasi-static simulations. Furthermore, there are no clear theoretical guidelines on the required mesh density. Considering the softening effects and mesh-dependent failure algorithms, trial-and-error is the only reasonable methodology to find the most appropriate mesh size while comparing the results against a controlled test data. Subsequently, it is possible to arrive at an optimum by experimenting with different meshing and developing some guidelines for that particular case. Material properties are mesh dependent; validation of a material model needs to include mesh density in the final model. LLNL-2 parameters are tuned for a mesh density of 1/80"/element and LLNL-3 parameters are tuned for a mesh density of 1/36"/element [3 and 4].

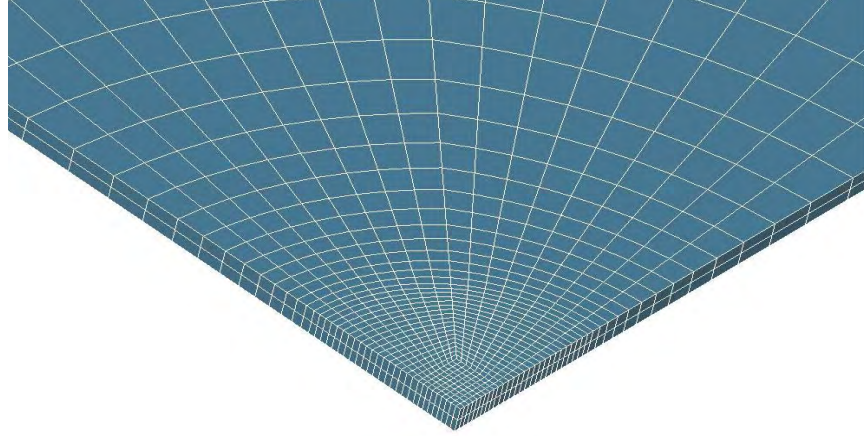


Figure 3. Close-Up of the Mesh-I, Coarse Mesh, 1/16" Target Model

In this study, the 1/16" target was modeled with 2 and 4 elements through-the-thickness, 1/8" plate was modeled with 4 and 8 elements through-the-thickness and the 1/4" plate was modeled with 8 and 16 elements through-the-thickness, respectively. Therefore, the element lengths through-the-thickness were 1/32" and 1/64" for the coarse and finer meshes, correspondingly. The coarse mesh is labeled as "Mesh-I" and the fine mesh is labeled as "Mesh-II," subsequently in this report. Figures 4 and 5 illustrate the close-ups of the 1/16" and 1/4" targets with Mesh-I and Mesh-II, respectively, where the mesh pattern was kept the same for the thicker targets, and only the number of elements were increased through-the-thickness.



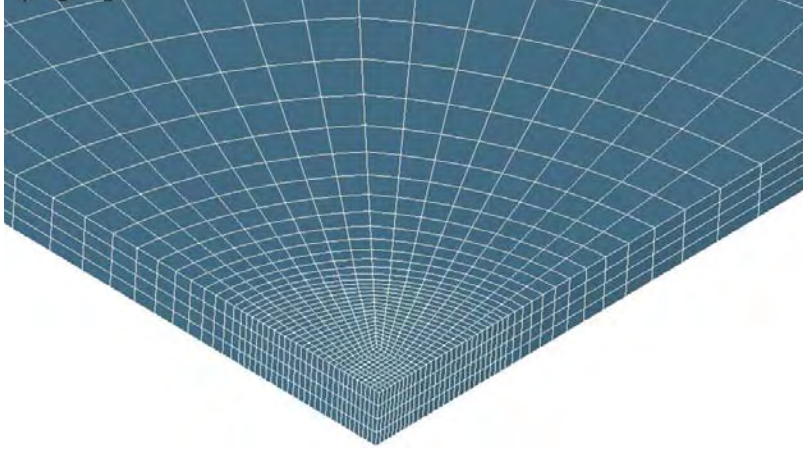


Figure 4. Close-Up of the Mesh-II, Fine Mesh, 1/16" Target Model

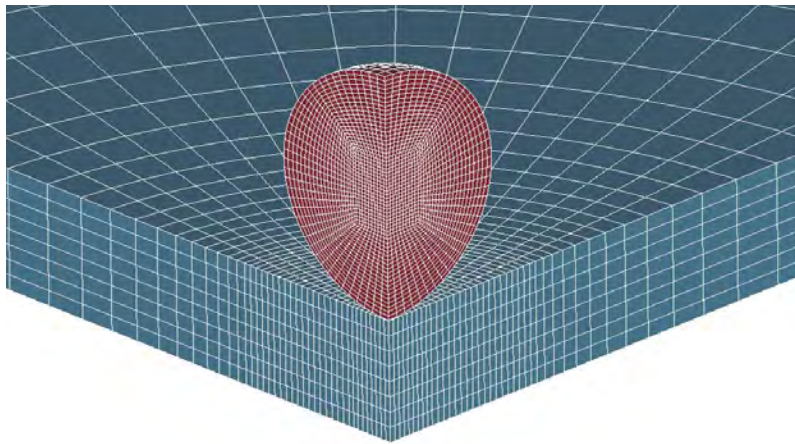


Figure 5. Close-Up of the Mesh-I, Coarse Mesh, 1/4" Target Model

### 3.1.2 Model With Spherical Projectile for Mesh Pattern Dependency.

Another FE model, which is labeled “Mesh-III” (shown in figure 6), was created by GWU to investigate the mesh pattern dependency. The concentric circular layers of the target were divided into three regions in the radial direction, and the mesh density gradually coarsens from inner region, which was the potential impact region, to the outer region. Mesh transition between the regions was good enough to prevent stress wave reflections from the boundary of regions. The target and the projectile were meshed with explicit 8-noded hexagonal elements of varying sizes. Three through-the-thickness elements were chosen to serve as a baseline since implementation of reduced integration solid elements requires at least three elements through-the-thickness to capture accurate bending deformation modes. Table 1 shows a comparison of the FE model sizes. The number of elements through-the-thickness is doubled for the 1/8" and 1/4" versions of the targets. As shown in table 1, the third mesh type (Mesh-III) is denser at the in-plane direction, which has three elements through-the-thickness. The number of through-the-thickness elements in Mesh-III is in between the two other meshes to judge whether in-plane or

through-the-thickness mesh density has more influence on the performance of ballistic limit predictions.

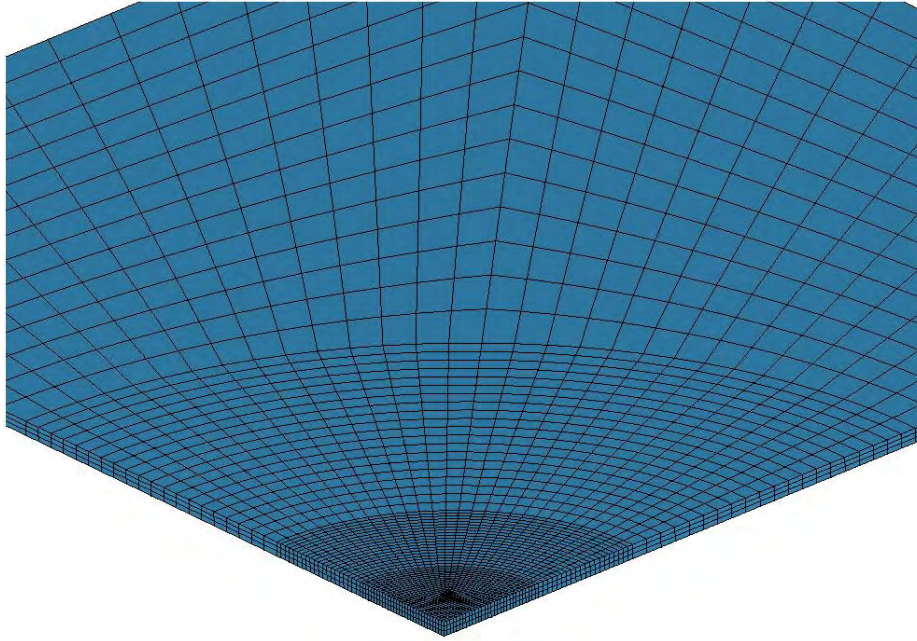


Figure 6. Close-Up of the Mesh-III, 1/16" Target Model

Table 1. The FE Models and Corresponding Model Sizes

Mesh Type	Developed By	Symmetry Assumption	Total Number of Elements at the Target			Number of Elements Through-the-Thickness			Target Mesh Density/Through-the-Thickness (inch/element)
			1/16"	1/8"	1/4"	1/16"	1/8"	1/4"	
Mesh-I	Boeing	3D - 1/4	1674	3348	6696	2	4	8	1/32
Mesh-II	Boeing	3D - 1/4	3348	6696	13392	4	8	16	1/64
Mesh-III	GWU	3D - 1/4	6975	13950	27900	3	6	12	1/48

### 3.1.3 Model With Cylindrical Projectile.

The impact area was modeled with a circular pattern, and therefore, the cylindrical projectile models can be easily compared with spherical models. The cylindrical projectile was also modeled in the same way as the spherical projectile so that the impact area (projected area) and the mass were the same in order to compare the results with test data with the same initial energy. Figure 7 shows the cylindrical model for 1/4" target and the coarser meshing pattern, Mesh-I.

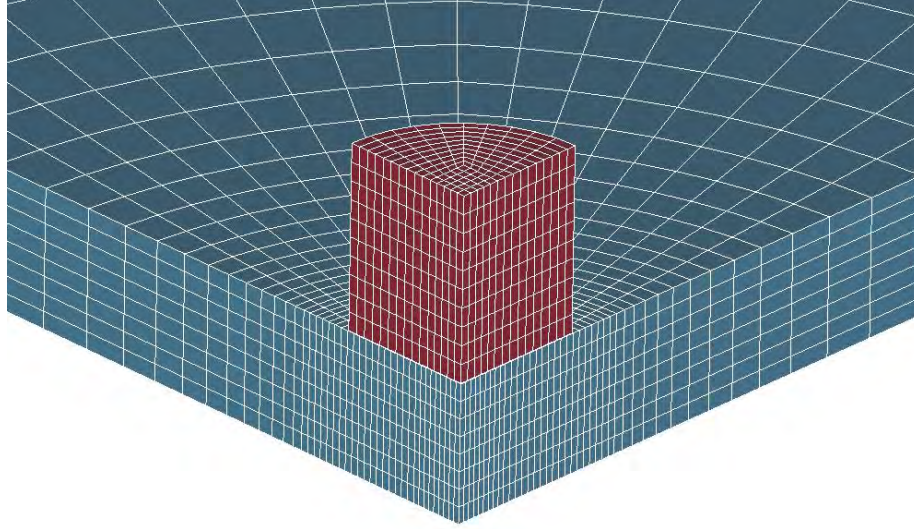


Figure 7. A 1/4" Target With Cylindrical Projectile, Mesh-I

#### 3.1.4 Model With Prismatic Projectile.

The impact area in this case is a square, and therefore, the target mesh pattern was chosen to be similar with the projectile. Figure 8 shows the cubical model for the 1/4" target and the coarser meshing pattern, Mesh-I.

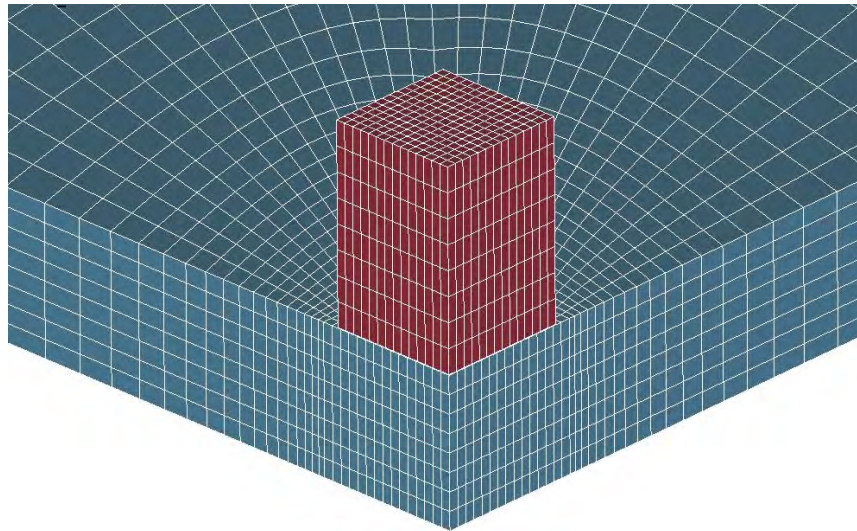


Figure 8. A 1/4" Target With Prismatic Projectile, Mesh-I

### 3.2 MATERIAL MODEL.

The steel projectile was modeled with 8-node solid elements using the linear elastic (\*MAT\_ELASTIC) material. The model does not allow plastic yielding but can have large deformations. Plasticity was unnecessary for this study, because neither the tests nor the early



runs showed any signs of yielding in the projectile. A more sophisticated material model was necessary for the targets to simulate ballistic impact response.

### 3.2.1 The J-C Material Model.

The J-C material model (\*MAT\_JOHNSON\_COOK) or (\*MAT\_15) was used for the aluminum targets. J-C is a strain rate and temperature-dependent (adiabatic assumption) visco-plastic model. It was employed to describe the response of 2024-T3/T351 aluminum. The J-C model represents the flow stress with an equation of the form [8-11]:

$$\sigma_y = \left( A + B\varepsilon^n \right) \left( 1 + C \ln \dot{\varepsilon}^* \right) \left( 1 - T^{*m} \right) \quad (1)$$

where  $\sigma_y$  is the effective stress,  $\varepsilon$  is the effective plastic strain,  $\dot{\varepsilon}^*$  is the normalized effective plastic strain rate (typically normalized to a strain rate of  $1.0 \text{ s}^{-1}$ ),  $n$  is the work hardening exponent and  $A$ ,  $B$ ,  $C$ , and  $m$  are material constants, where their physical meanings are described in table 2. The quantity  $T^*$  is defined as:

$$T^* = \frac{T - T_{room}}{T_{melt} - T_{room}} \quad (2)$$

where  $T_{room}$  is the room temperature,  $T_{melt}$  is the melting temperature and is typically taken as the solidus temperature for an alloy. For high rate deformation problems, it is assumed that an arbitrary percentage of the plastic work done during deformation produces heat in the deforming material. For many materials, 90-100 percent of the plastic work was dissipated as heat in the material. Thus, the temperature used in equation 1 can be derived from the increase in temperature according to the following expression:

$$\Delta T = \frac{\alpha}{\rho c} \int \sigma(\varepsilon) d\varepsilon \quad (3)$$

where  $\Delta T$  is the temperature increase,  $\alpha$  is the percentage of plastic work transformed to heat,  $c$  is the heat capacity and  $\rho$  is the density.

Damage in the J-C material model is based on a cumulative damage law:

$$D = \sum \frac{\Delta \varepsilon}{\varepsilon_f} \quad (4)$$

in which effective plastic strain at failure is defined as:

$$\varepsilon_f = \left[ D_1 + D_2 \exp(D_3 \sigma^*) \right] \left[ 1 + D_4 \ln \dot{\varepsilon}^* \right] \left[ 1 + D_5 T^* \right] \quad (5)$$

where  $\Delta\varepsilon$  is the increment of effective plastic strain during an increment in loading, and  $\sigma^*$  is the mean stress normalized by the effective stress, which is often referred as triaxiality. The parameters  $D_1$ ,  $D_2$ ,  $D_3$ ,  $D_4$ , and  $D_5$  are fracture constants. Failure of elements is assumed to occur when  $D = 1$ . The failure strain  $\varepsilon_f$ , and thus the accumulation of damage, is a function of stress triaxiality, strain rate, and temperature. Failed elements are removed from the FE model with an element erosion algorithm. The J-C material model was used in conjunction with Mie-Gruneisen equation of state (EOS) model.

### 3.2.2 Mie-Gruneisen EOS.

Mie-Gruneisen EOS model defines the pressure volume relationship in one of two ways, depending on whether the material is compressed or expanded. The Mie-Gruneisen EOS model, with cubic shock velocity-particle velocity, defines pressure for compressed materials as:

$$p = \frac{\rho_0 C_{sp}^2 \mu \left[ 1 + \left( 1 - \frac{\gamma_0}{2} \right) \mu - \frac{a}{2} \mu^2 \right]}{\left[ 1 - (S_1 - 1) \mu - S_2 \frac{\mu^2}{\mu + 1} - S_3 \frac{\mu^3}{(\mu + 1)^2} \right]} + (\gamma_0 + a\mu) E_{int} \quad (6)$$

and for expanded materials as:

$$p = \rho_0 C_{sp}^2 \mu + (\gamma_0 + a\mu) E_{int} \quad (7)$$

where  $E_{int}$  is internal energy,  $C_{sp}$  is the intercept of the vs-vp curve;  $S_1 - S_3$  are the coefficients of the slope of the vs-vp curve,  $\gamma_0$  is the Gruneisen gamma,  $a$  is the first-order volume correction to  $\gamma_0$ , and  $\mu$  is given as:

$$\mu = \frac{\rho}{\rho_0} - 1 \quad (8)$$

### 3.2.3 Material Characterization.

Four different sets of material model parameters are listed for 2024-T3/T351 in table 2. These parameters were found through literature [1] and LLNL material characterization tests [2-4]. The yield surfaces for these sets of parameters are illustrated in figure 9. The yield surface for LLNL-1, LLNL-2, and LLNL-3 used the same strength constants. The damage model constants are also listed in table 2, and the differences in fracture locus are illustrated in figure 10, with respect to stress triaxiality at a nominal strain rate of 1/s. LLNL-2 and LLNL-3 differ from the rest by considering a recalibration of the parameters with the ballistic impact test results from LLNL and UCB. Since the type of failure mode is subject to change from petaling to plugging due to the change in thickness, the same set of damage constants do not work for the whole range of material thickness [4 and 6]. Optimization and tuning is necessary to find the best set of parameters that work reasonably well for the other thicknesses. The predictive performance of these parameters is given in the proceeding sections.

Table 2. The J-C Material Model Parameters

Parameter	Notation	Literature [1]	LLNL-1 [2]	LLNL-2 [3]	LLNL-3 [4]
Strength Parameters					
Density (lb/in. <sup>3</sup> ), [kg/m <sup>3</sup> ]	$\rho$	0.100434 [2770]	0.100434 [2770]	0.100434 [2770]	0.100434 [2770]
Poisson Ratio	$\nu$	0.33	0.33	0.33	0.33
Modulus of Elasticity (psi), [MPa]	$E$	1.06E+7 [73084]	1.06E+7 [73084]	1.06E+7 [73084]	1.06E+7 [73084]
Static Yield Limit (psi), [MPa]	$A$	38400 [265]	53517 [369]	53517 [369]	53517 [369]
Strain Hardening Modulus (psi), [MPa]	$B$	61800 [426]	99202 [684]	99202 [684]	99202 [684]
Strain Hardening Exponent	$n$	0.34	0.73	0.73	0.73
Strain Rate Coefficient	$C$	0.015	0.0083	0.0083	0.0083
Thermal Softening Exponent	$m$	1.0	1.7	1.7	1.7
Reference Temperature (°F), [°K]	$T_{room}$	69.5 [294]	69.5 [294]	69.5 [294]	69.5 [294]
Melting Temperature (°F), [°K]	$T_{melt}$	935 [775]	935 [775]	935 [775]	935 [775]
Specific Heat (in. <sup>2</sup> /s <sup>2</sup> -°F), [J/kg-°K]	$c_p$	754000 [875]	754000 [875]	754000 [875]	754000 [875]
Damage Parameters					
$D_1$		0.13	0.13	0.112	0.31
$D_2$		0.13	0.13	0.123	0.045
$D_3$		-1.5	-1.5	-1.5	-1.7
$D_4$		0.011	0.011	0.007	0.005
$D_5$		0	0	0	0
Mie-Grunesien EOS Parameters					
$S_1$		1.338	1.338	1.338	1.338
$S_2$		0	0	0	0
$S_3$		0	0	0	0
$\gamma_0$		2	2	2	2
$a$		0.48	0.48	0.48	0.48

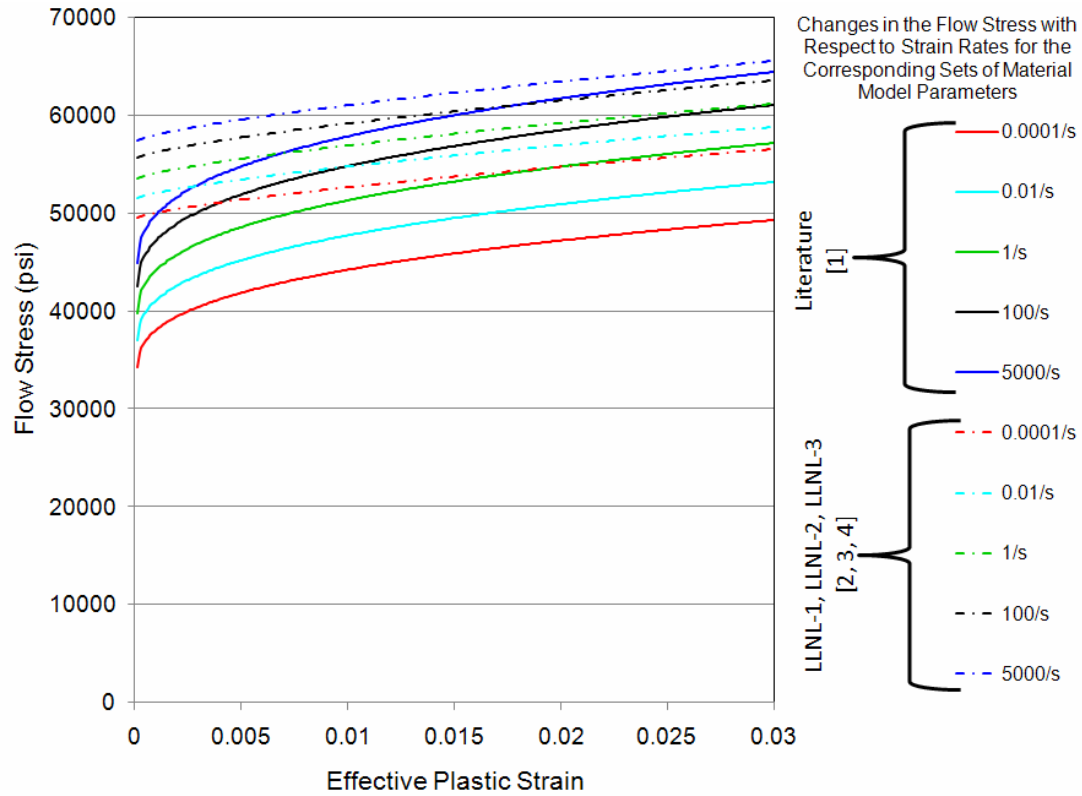


Figure 9. Differences in the Yield Surface Data for 2024-T3/T351

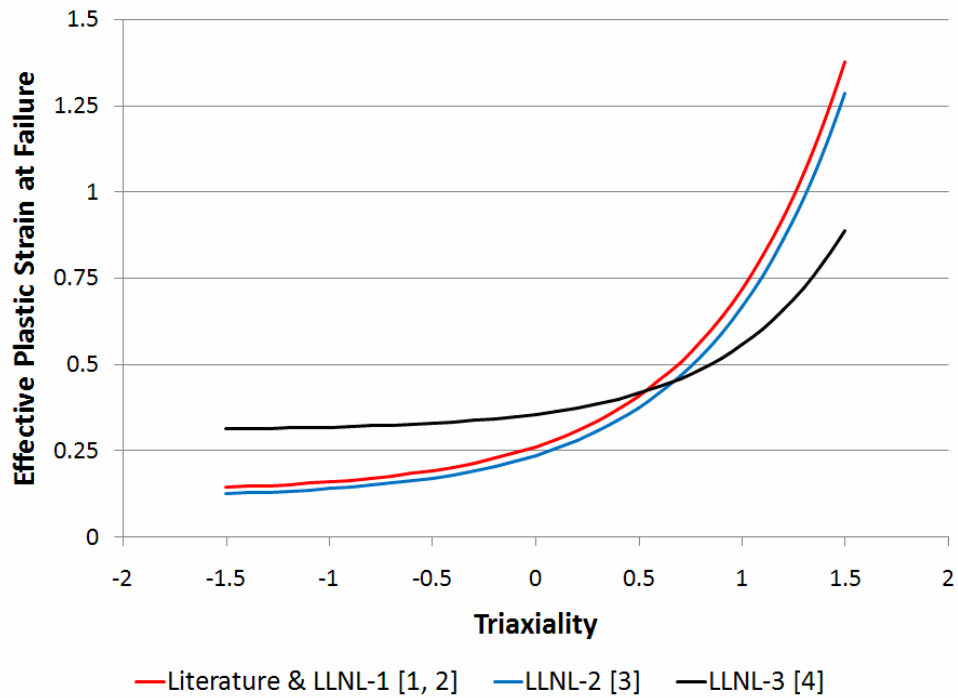


Figure 10. Differences in the Fracture Locus Data for 2024-T3/T351

### 3.3 BULK VISCOSITY.

Bulk viscosity is a numerical way to handle pressure waves in material by applying an additional additive pressure in the form of [11]:

$$\begin{aligned} q &= \rho l (Q_1 l \dot{\epsilon}_{kk}^2 - Q_2 a \dot{\epsilon}_{kk}) & \text{if } \dot{\epsilon}_{kk} < 0 \\ q &= 0 & \text{if } \dot{\epsilon}_{kk} \geq 0 \end{aligned} \quad (9)$$

where  $q$  is a viscous term that is added to the pressure to smear the shock discontinuities into rapidly varying but continuous transition regions,  $l$  is the characteristic length given as the cube root of the volume for solid elements,  $a$  is the local sound speed in the material, and  $Q_1$  and  $Q_2$  are the corresponding dimensionless constants. The overall effect to the model is that it dissipates energy from the system with a sense similar to damping. Within the impact velocities covered in this study, LSTC recommended that the default values should be increased. The default values and LSTC-recommended values for the linear and quadratic terms are given in table 3.

Table 3. Bulk Viscosity Coefficients

	Quadratic Term $Q_1$	Linear Term $Q_2$
Default	1.5	0.06
Recommended	2	0.1

### 3.4 CONTACT DEFINITIONS.

LS-DYNA offers a number of contact definition options. Furthermore, the chosen contact type needs user-defined input options, which can greatly affect the results. The following two contact options were used in this work:

- \*CONTACT\_ERODING\_SINGLE\_SURFACE with SOFT=1
- \*CONTACT\_ERODING\_SINGLE\_SURFACE with SOFT=2

SOFT=1 used the nodal constraint formulation and SOFT=2 used the segment-based constraint option. Other contact types were also examined, but these two were found to be the most appropriate for the high-speed impacts that are simulated in this study.

The default LS-DYNA input parameters were used, except SBOPT=5 with SOFT=2, which includes warped segment checking and sliding during a segment-based contact option. The element sizes on both the projectile and target sides were approximately the same as those recommended by LSTC. Since the projectile is made of steel and the target is aluminum, the material stiffness on both sides in contact was relatively similar. The static and dynamic coefficients of friction were 0.5 between aluminum target and steel projectile.

In general, all these contact options were stable throughout the analysis runs.



### 3.5 NONLOCAL FAILURE.

During the ballistic impact simulations, failure can be localized, and mesh size and pattern plays an important role. Nonlocal theories were adopted for the numerical solvers to reduce this mesh sensitivity. In this study, the performance of the nonlocal option was examined. The choice of the characteristic length,  $L$ , is important while using the nonlocal option. Using a smaller length may have no effect in the results, but choosing a larger value may cause extreme computational cost. Usually, a length that spans the integration points of the neighboring elements is preferred, as shown in figure 11.

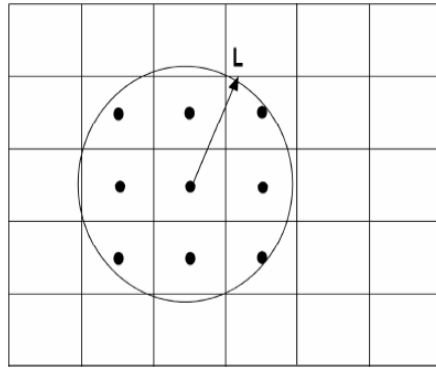


Figure 11. Determination of the Characteristic Length for Nonlocal Failure Option

### 3.6 COMPUTING PLATFORMS.

All FE simulations were carried out with Version 970 of LS-DYNA. The computations were performed on the Boeing Linux CP cluster in Bellevue, WA, and on the SGI<sup>®</sup> Origin<sup>®</sup> 3600 supercomputer at GWU. Cross-platform checks were done for a number of cases and good agreement was achieved between the platforms.

## 4. BALLISTIC IMPACT SIMULATION RESULTS FOR DIFFERENT MESHES.

Ballistic impact response for three different material thicknesses was examined with different options. For each thickness, the Boeing Mesh-I and Mesh-II and GWU Mesh-III were compared to examine the interaction of the material model parameters with the mesh pattern and size by employing LLNL-2 and LLNL-3 material model parameters.

In addition, for each thickness, the effects of using segment-based contact with SOFT=2 and nonlocal smoothing is compared for Mesh-I and Mesh-II to examine whether the contact and smoothing options have a significant effect on the performance while LLNL-3 material model parameters were employed.

The responses are illustrated by generating initial velocity versus residual velocity graphs, where they can be compared to the UCB ballistic test data. The reference line in each graph represents the condition if impact and exit velocities are the same, which indicates no loss in the energy.

Therefore, the distance between the reference line and the data line can be accepted as the velocity or energy lost during the penetration.

#### 4.1 TARGET THICKNESS 1/16".

The penetration through the 1/16" aluminum target is illustrated in figure 12, and the comparison between the measurements and computations is shown in figures 13 to 16. A petaling type of deformation mode was observed. There was significant local bending in the target and material failed mostly in tension. It should be noted that the plug was pushed out in front of the sphere, and there were three radial cracks in the target. The failure mode, the plug formation, and the radial cracks all correspond well with the test results.

It was observed that the LLNL-2 material data gave excellent correlation, but the LLNL-3 data with new failure parameters did not agree as well with the test results for either mesh patterns. This deviation from the test results while using the LLNL-3 material model parameters can be explained by the fact that these parameters were adjusted for thicker targets and may not necessarily be appropriate for thinner samples since mesh size and target thickness affect the accuracy.

The segment contact and nonlocal material definitions did not seem to provide any improvement in the accuracy, but had an impact on the mesh dependency.

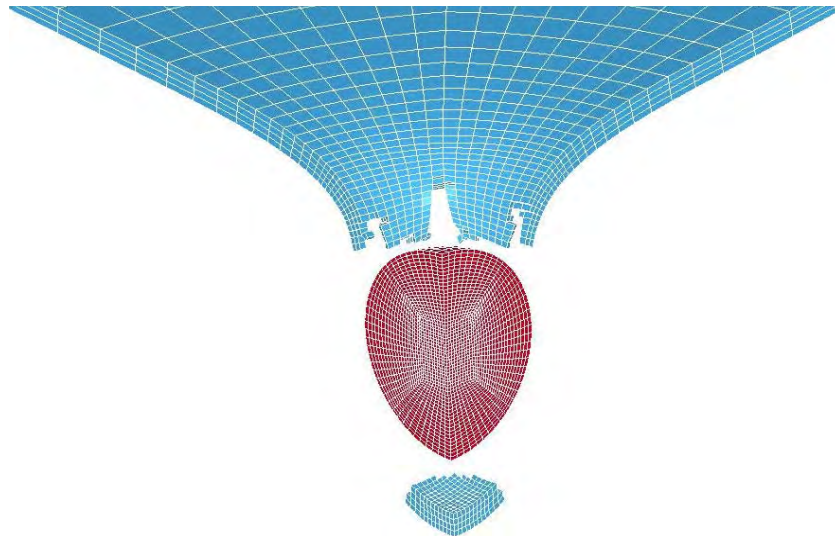


Figure 12. Penetration Through 1/16" Target and Petal Formation

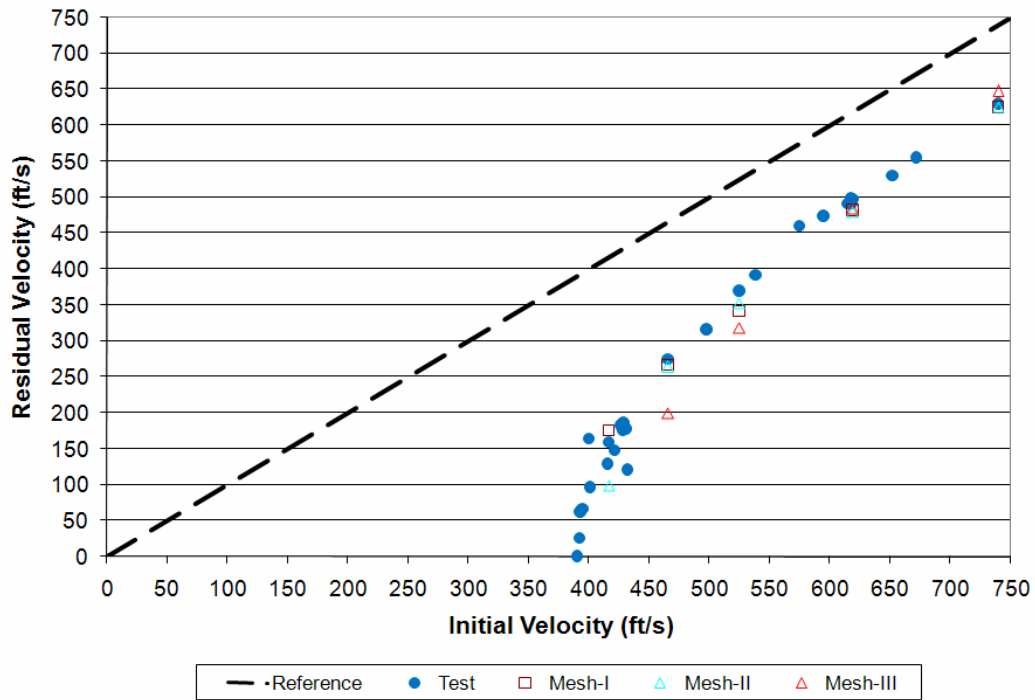


Figure 13. Ballistic Limit Predictions for LLNL-2 Material Data, 1/16" Target

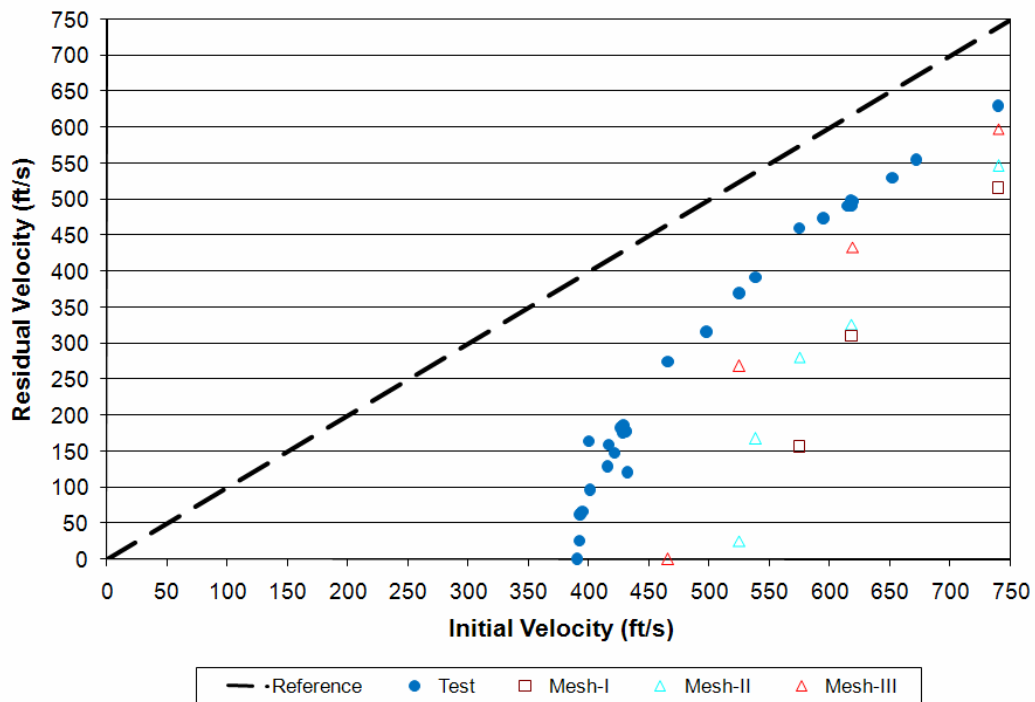


Figure 14. Ballistic Limit Predictions for LLNL-3 Material Data, 1/16" Target

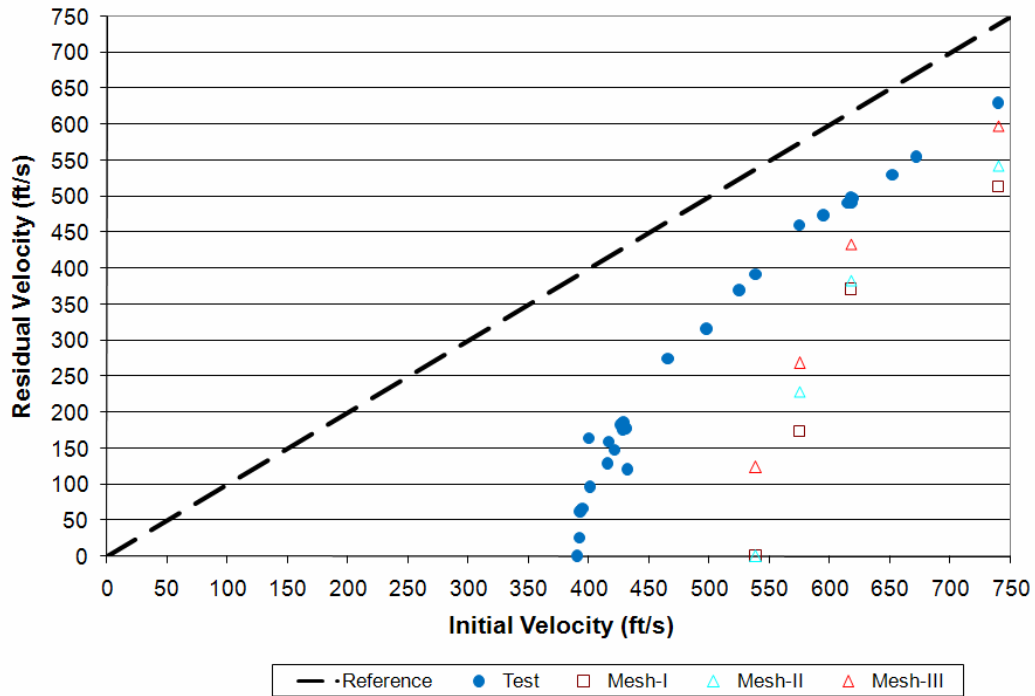


Figure 15. Ballistic Limit Predictions for LLNL-3 Material Data, 1/16" Target

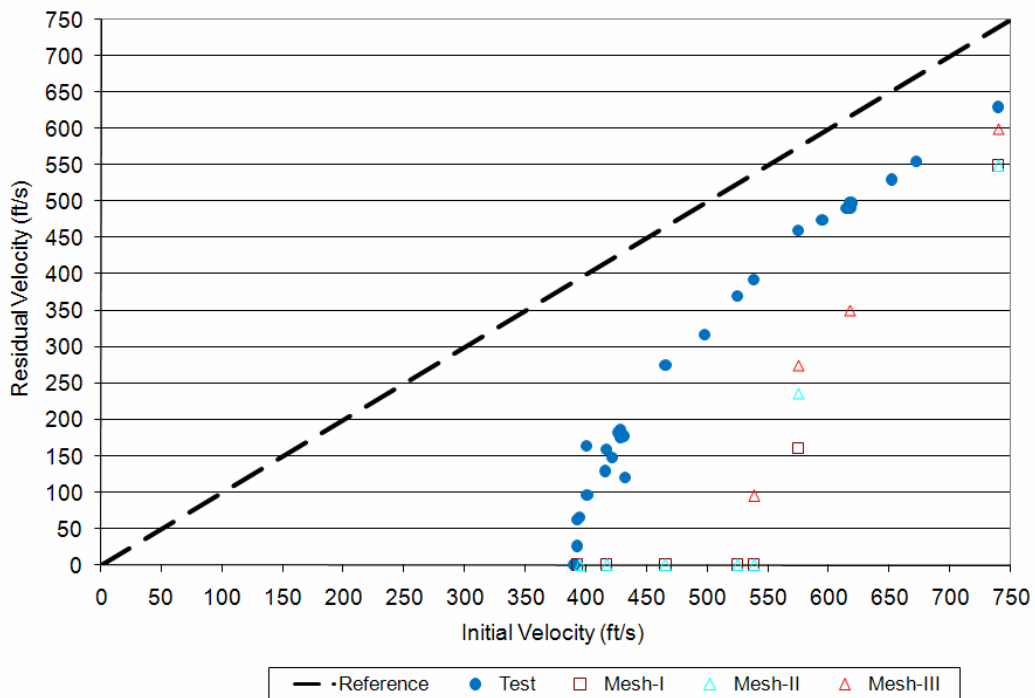


Figure 16. Ballistic Limit Predictions for LLNL-3 Material Data With Nonlocal Smoothing, 1/16" Target

## 4.2 TARGET THICKNESS 1/8".

The penetration through 1/8" aluminum target is shown in figure 17, and the comparison between the measurements and computations is shown in figures 18 to 21. The projectile penetrated through the target in mixed mode: partly petaling and partly plugging. There was some local bending and some local shearing in the target; hence, the material failed partially in shear and partially in tension. Note that a plug was pushed out in front of the sphere and the size of the radial cracks in the target got smaller. The failure mode and plug formation correspond with the test results.

The LLNL-2 parameter simulations showed a relatively poor correlation with the test for all three mesh patterns. However, the LLNL-3 data, with newest failure parameters, agreed somewhat better with the test results. The employed material model parameters provided drastically different results; where the LLNL-2 parameters underpredicted the ballistic limit, the LLNL-3 overpredicted it. It should also be noted that this deviation was much more dependent on the material model parameters than on the mesh pattern or size sensitivity.

The segment contact and nonlocal material definitions seemed to decrease the accuracy for this set of analysis, but had an impact on the mesh dependency.

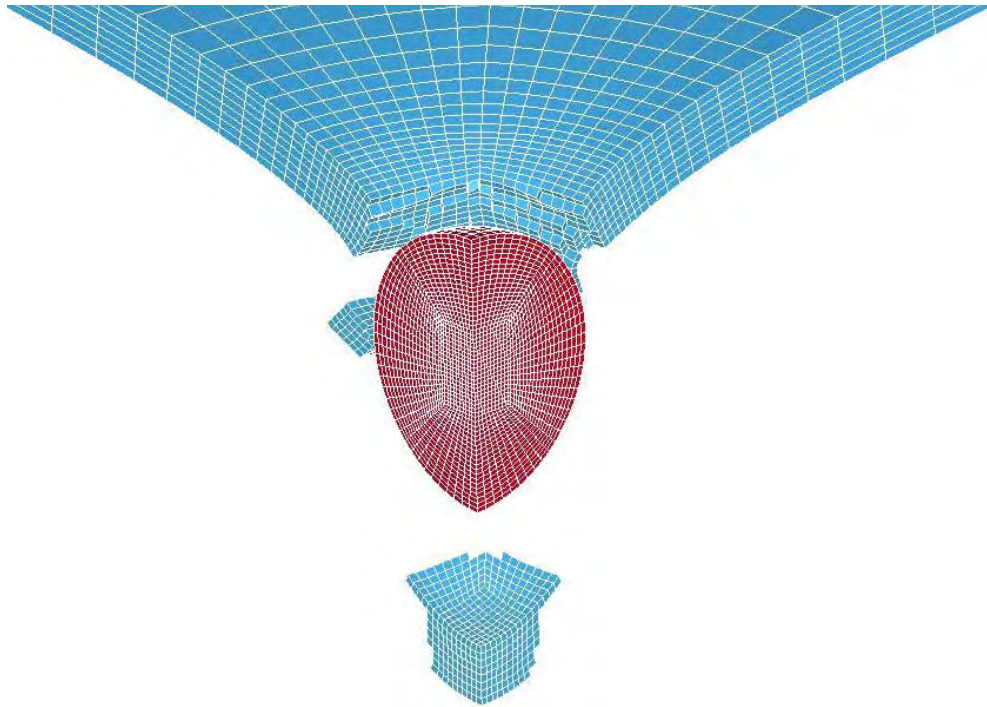


Figure 17. Penetration Through 1/8" Target and Mixed Mode Failure

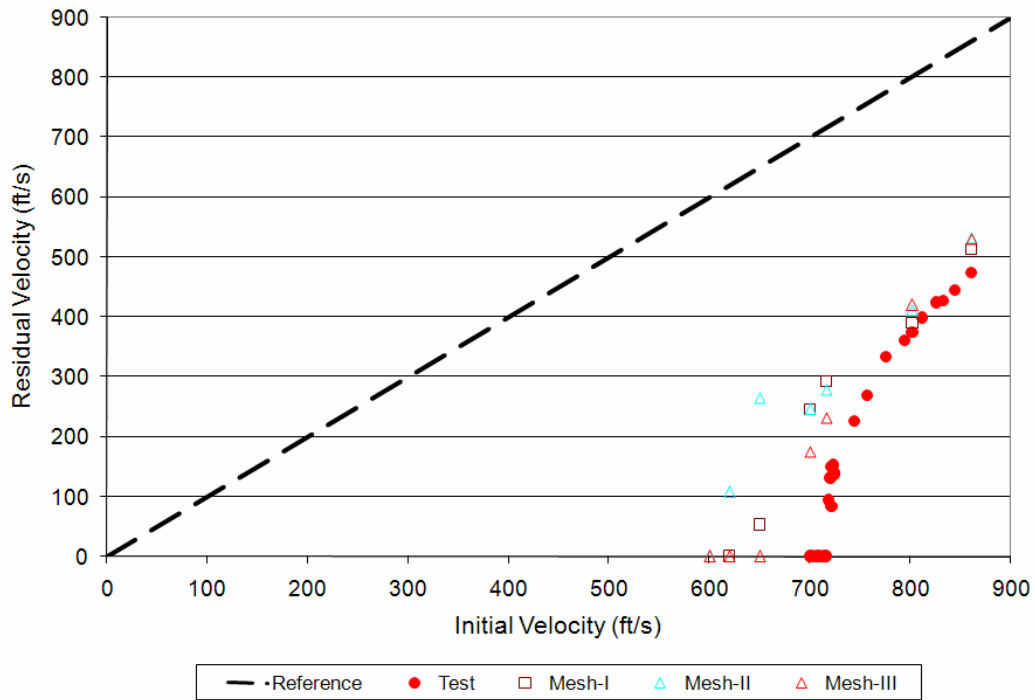


Figure 18. Ballistic Limit Predictions for LLNL-2 Material Data, 1/8" Target

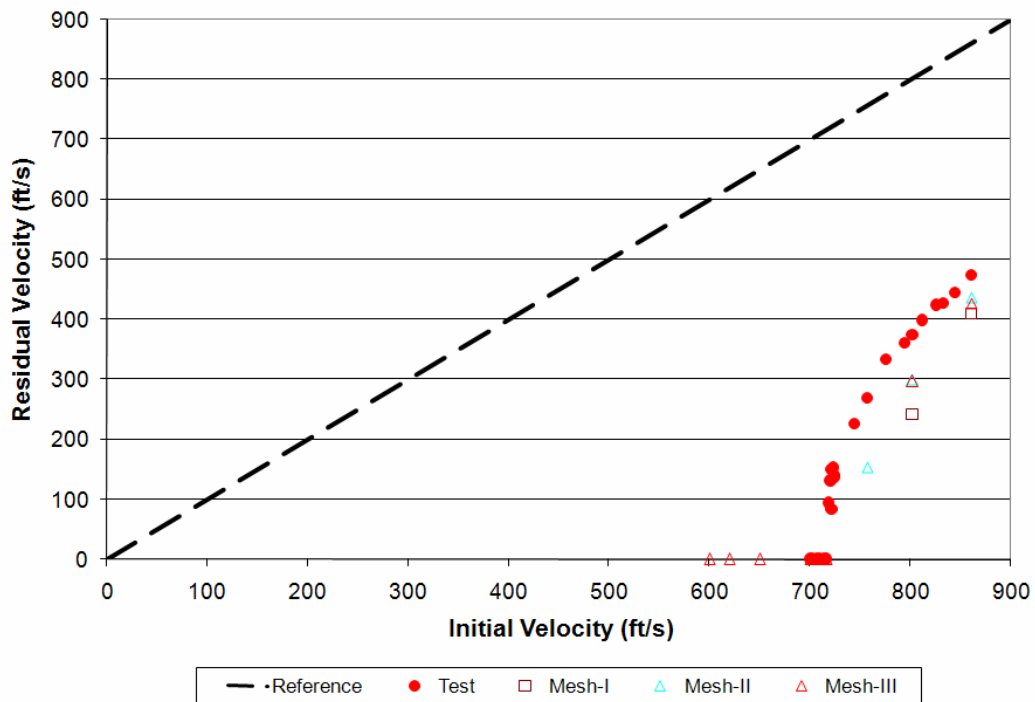


Figure 19. Ballistic Limit Predictions for LLNL-3 Material Data, 1/8" Target

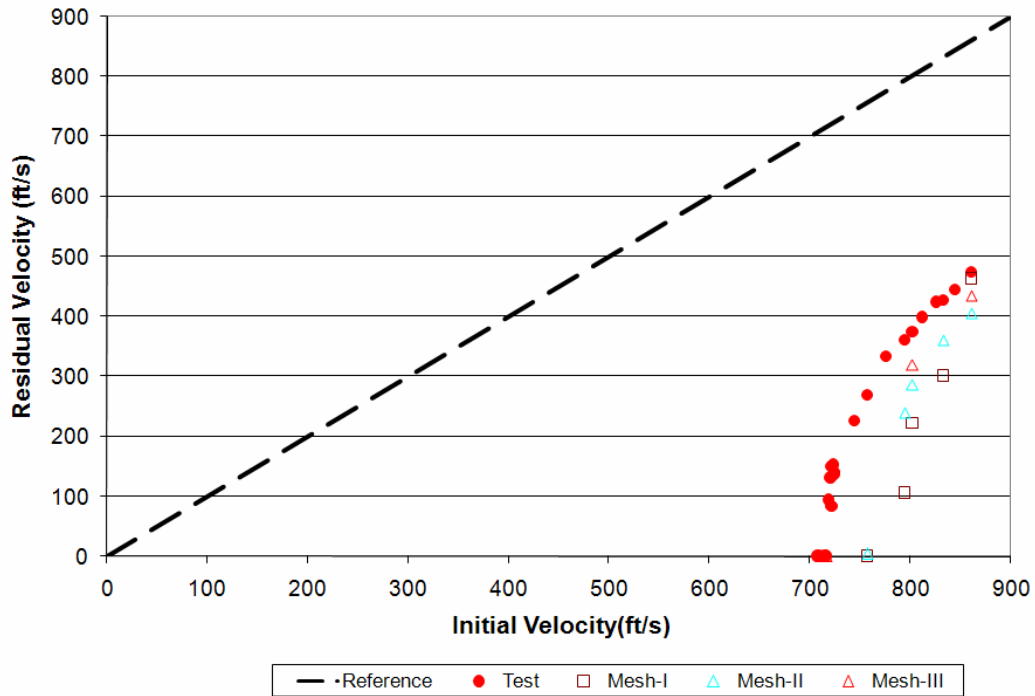


Figure 20. Ballistic Limit Predictions for LLNL-3 Material Data With Segment Contact, 1/8" Target

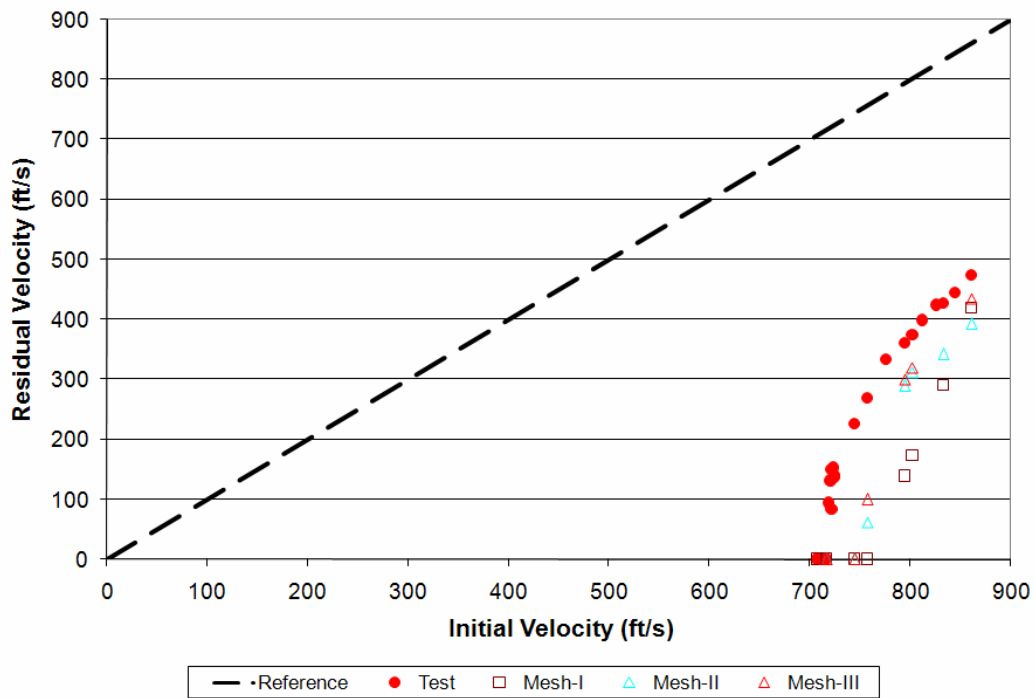


Figure 21. Ballistic Limit Predictions for LLNL-3 Material Data With Nonlocal Smoothing, 1/8" Target

### 4.3 TARGET THICKNESS 1/4".

The penetration through 1/4" aluminum target is shown in figure 22, and the comparison between the measurements and computations is shown in figures 23 to 26. The projectile penetrated the target in plugging mode. The material failed entirely in shear. Note that a plug was pushed out in front of the sphere, and there were no radial cracks in the target. The failure mode and the plug formation correspond with the test results.

The LLNL-2 material data showed a poor correlation to the test, but the LLNL-3 data with newest failure parameters correlated much better since they were specifically tuned for thicker targets.

The segment contact and nonlocal material definitions did not seem to make any difference.

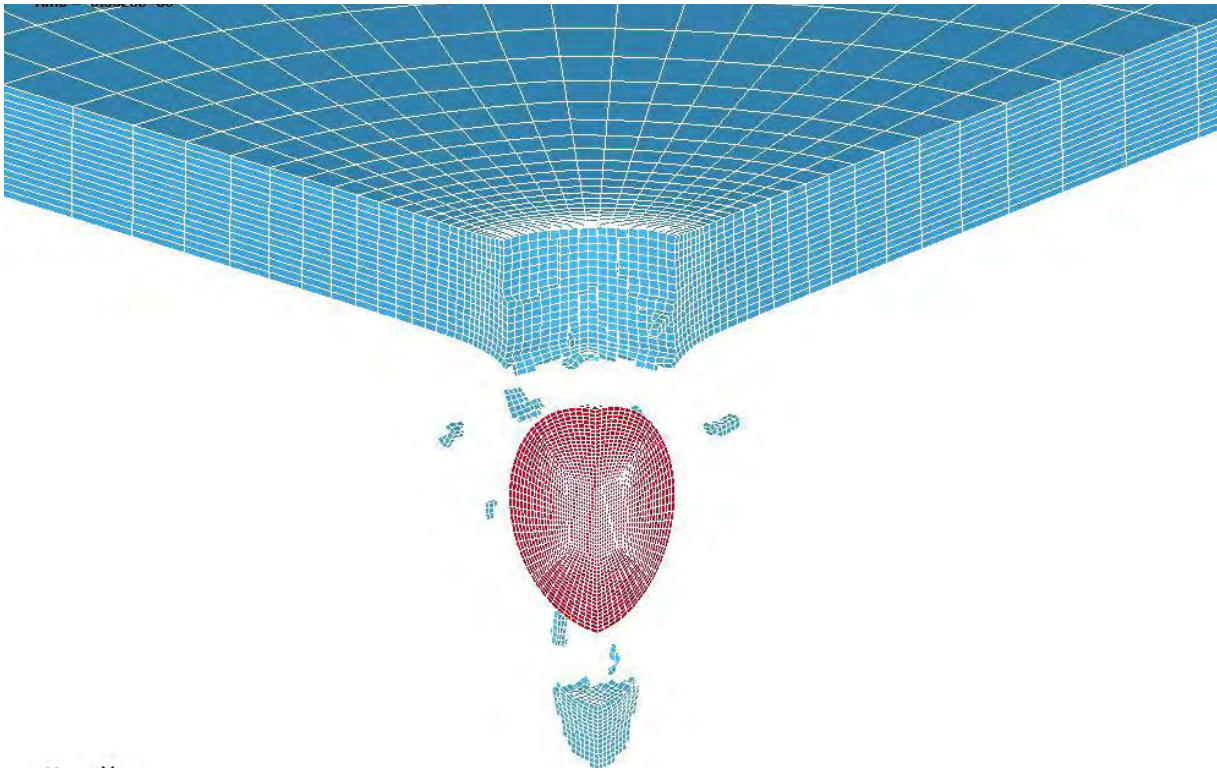


Figure 22. Penetration Through 1/4" Target and Plugging



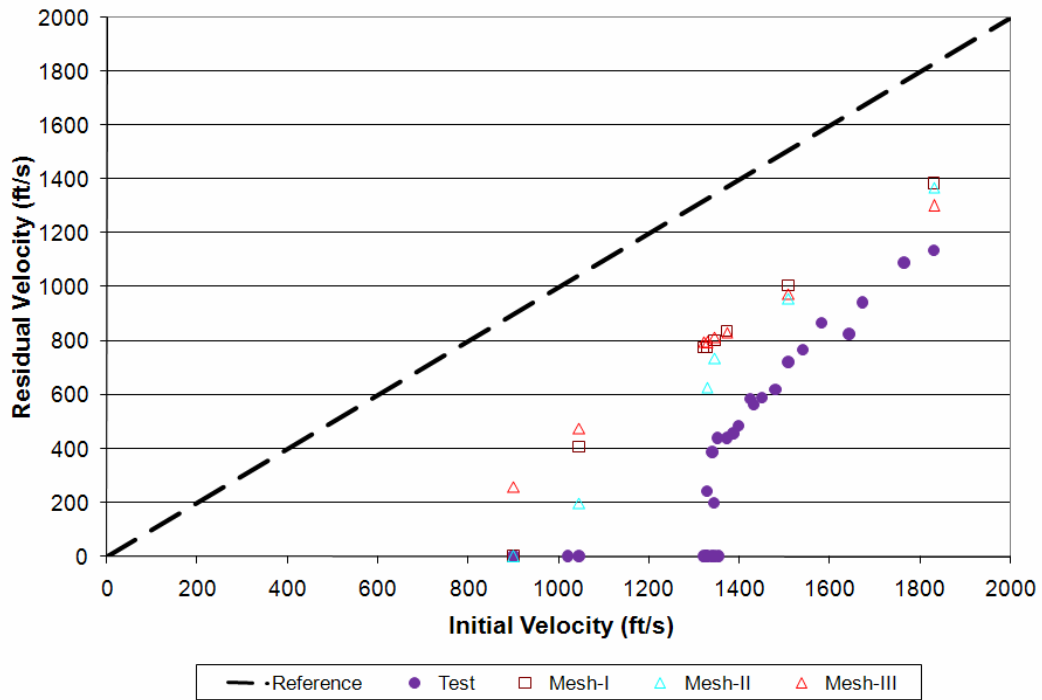


Figure 23. Ballistic Limit Predictions for LLNL-2 Material Data, 1/4" Target

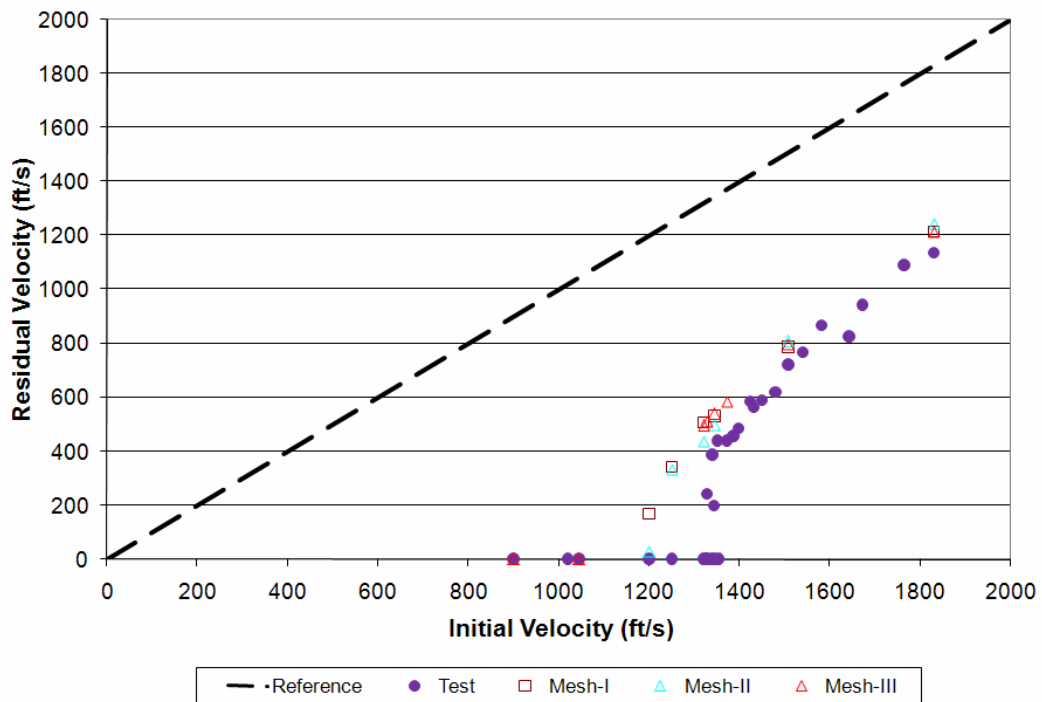


Figure 24. Ballistic Limit Predictions for LLNL-3 Material Data, 1/4" Target

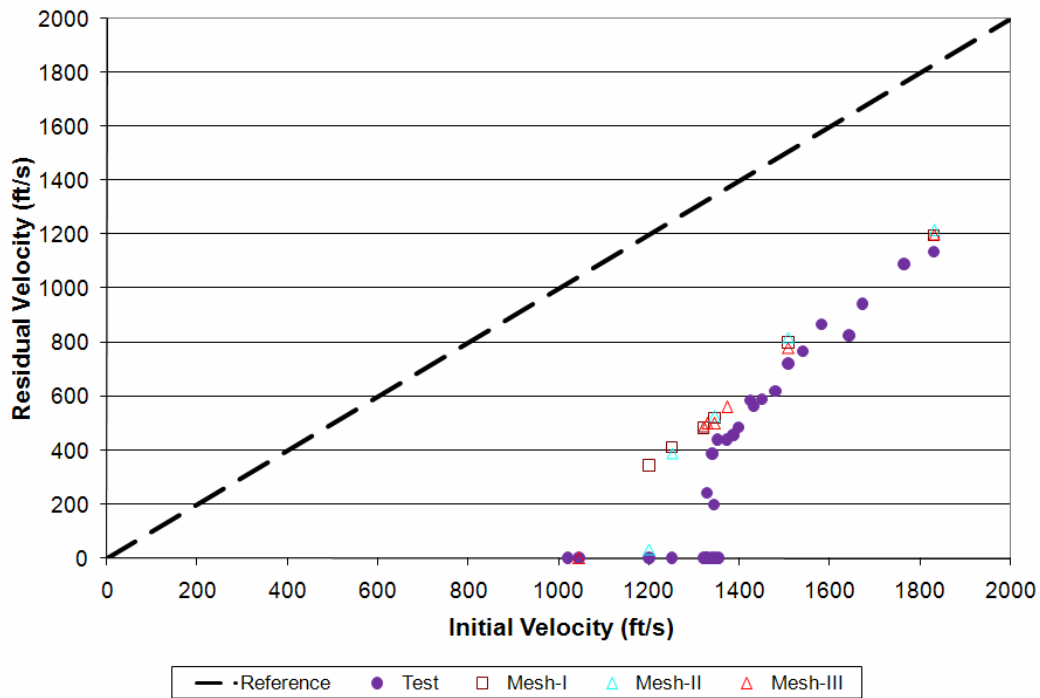


Figure 25. Ballistic Limit Predictions for LLNL-3 Material Data With Segment Contact, 1/4" Target

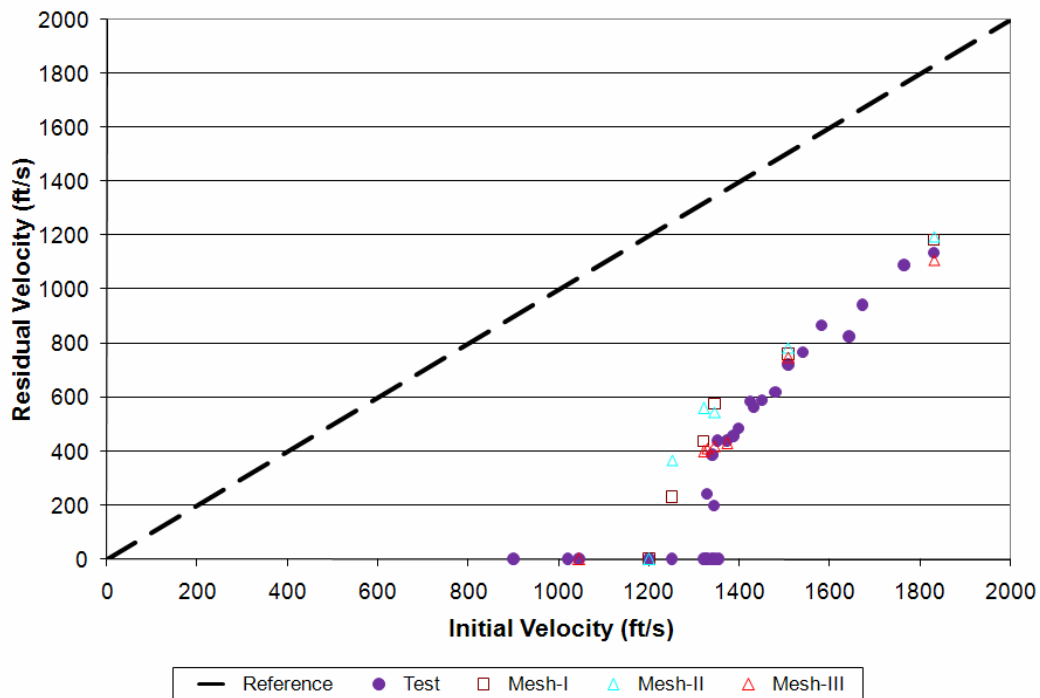


Figure 26. Ballistic Limit Predictions for LLNL-3 Material Data With Nonlocal Smoothing, 1/4" Target

## 5. THE EFFECTS OF MATERIAL MODEL PARAMETERS.

The effects of mesh dependency was less than the set of material model parameters employed in the material model as shown in section 4. Therefore, all four available material model parameters for 2024-T3/T351 aluminum material listed in table 2 were compared to find the best option. The penetration through the 1/16" target is illustrated in figures 27 and 28. As shown in the figures, petaling deformation occurred as the spherical projectile penetrated the material, where a significant amount of local bending caused failure in the state of tension. The type of radial crack formation with the plugging and petaling was successfully captured with the simulation. The predictive capability of the different sets of material model parameters was compared, as shown in figure 29, for this thickness. Each of the four sets of parameters were found to be in fairly good agreement with the test results, where LLNL-2 set was found to be the most accurate of the four for the test cases used in this study.

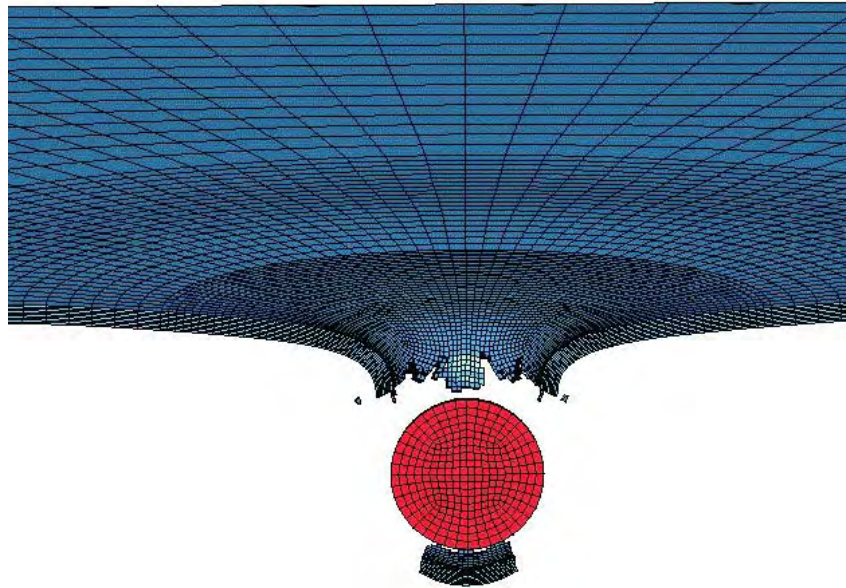


Figure 27. Ballistic Impact Simulation for 1/16" 2024-T3 Target



Figure 28. Ballistic Impact Test Results for 1/16" 2024-T3 Target (a) Front and (b) Rear View

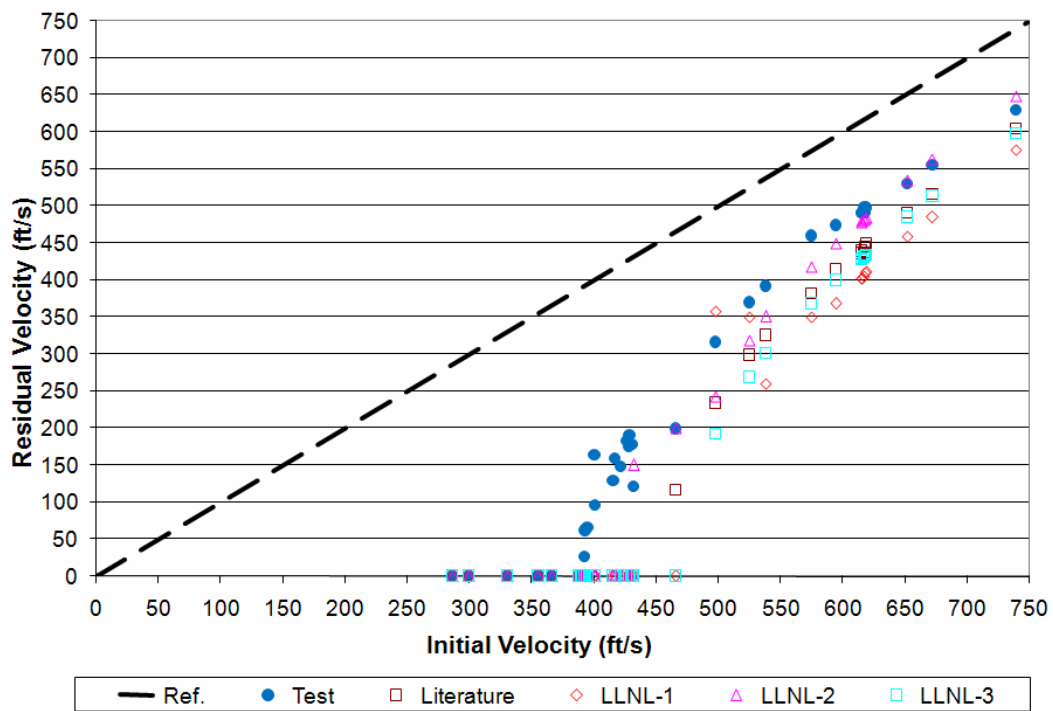


Figure 29. Ballistic Limit Predictions (Mesh-III) for 1/16" 2024-T3

The penetration through 1/8" target is illustrated in figures 30 and 31, where a mixed mode type of deformation occurred as the spherical projectile penetrated the material and, consequently, the material failed partially in shear and partially in tension. The sizes of the radial cracks were not significant, and partial petaling was observed with partial plugging formation. Figure 32 shows

a comparison of the predictive capability of the different sets of material model parameters for this thickness. The damage parameters failed to capture the transition region in deformation and failure, where LLNL-3 set was found to be the most accurate among the others.

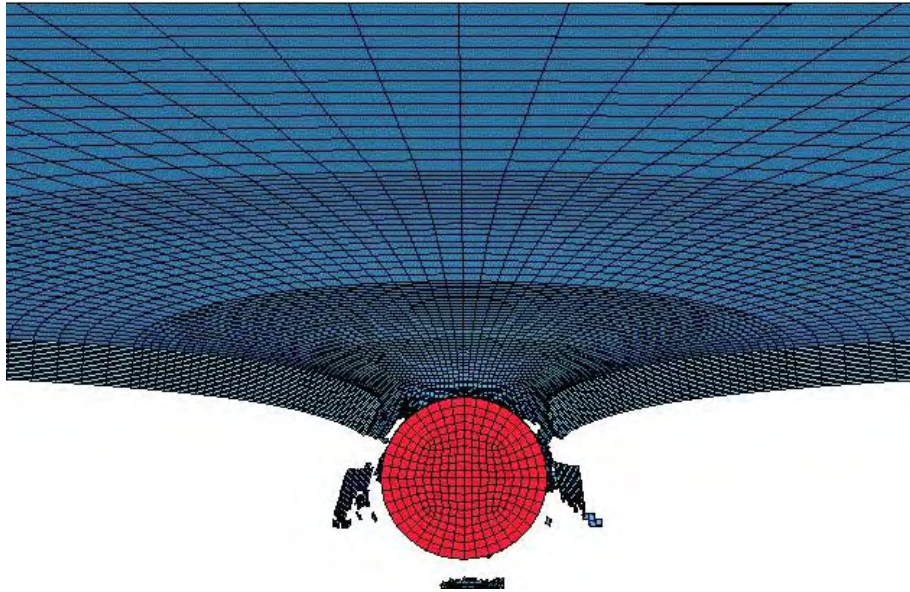
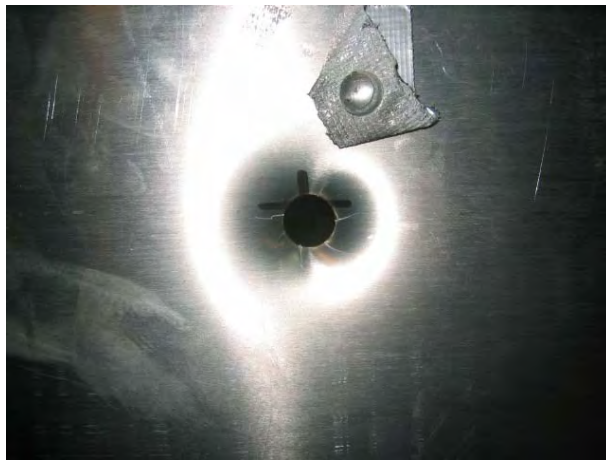


Figure 30. Ballistic Impact Simulation for 1/8" 2024-T3 Target



(a)



(b)

Figure 31. Ballistic Impact Test Result for 1/8" 2024-T3 Target (a) Front and (b) Rear View

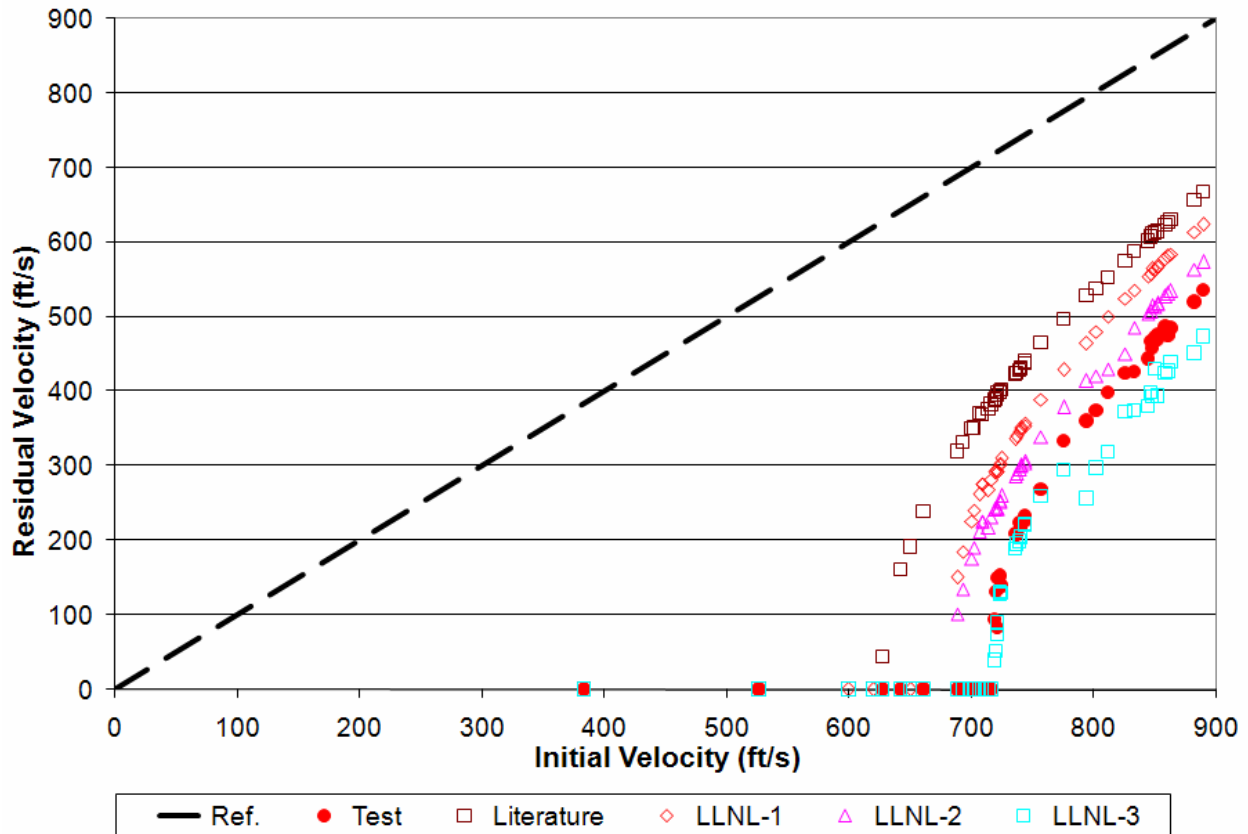


Figure 32. Ballistic Limit Predictions (Mesh-III) for 1/8" 2024-T3

The penetration through 1/4" target is illustrated in figures 33 and 34. Plugging mode deformation occurred as the spherical projectile penetrated the material and the material failed entirely in shear. No radial crack was observed. Figure 35 shows the comparison of the predictive capability of the different sets of material model parameters for this thickness. The damage parameters are further from the experiment with the exception of the LLNL-3 model, which has been tuned to model the thicker targets.



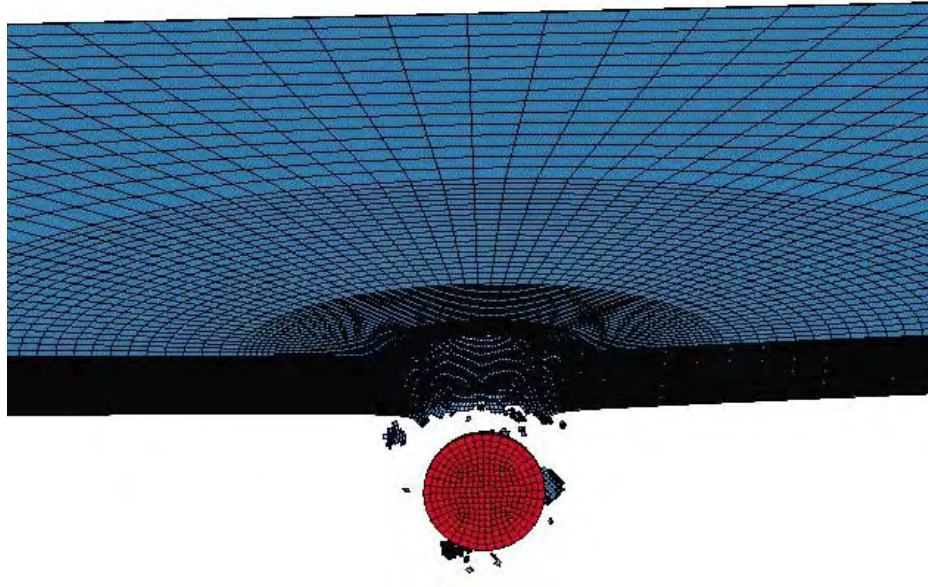
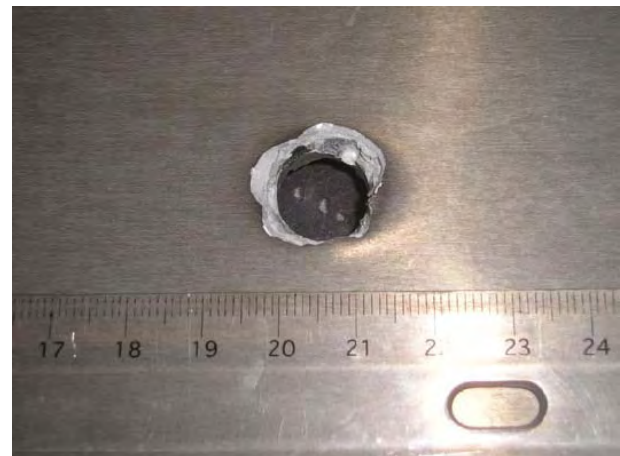


Figure 33. Ballistic Impact Simulation for 1/4" 2024-T351 Target



(a)



(b)

Figure 34. Ballistic Impact Test Results for 1/4" 2024-T351 Target  
(a) Front and (b) Rear View

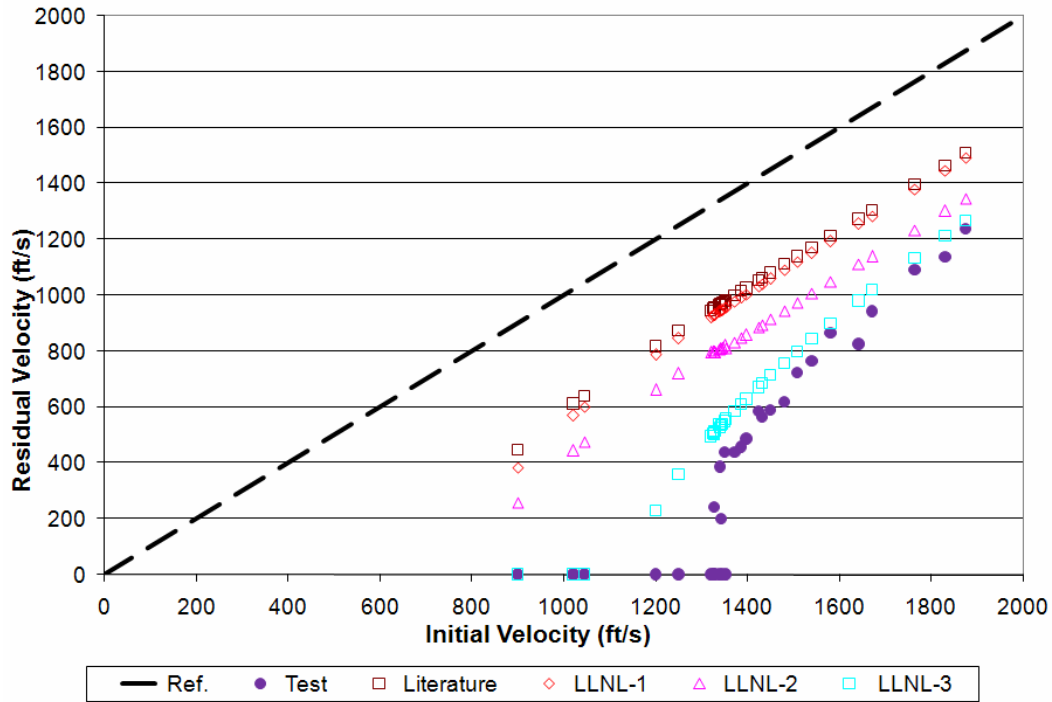


Figure 35. Ballistic Limit Predictions (Mesh-III) for 1/4" 2024-T351

### 5.1 PLATFORM DEPENDENCY AND COMPUTATIONAL COST.

Cross-platform consistency, robustness, and repeatability are major issues for ballistic impact simulations. Verification of the reliability between the computing platforms would provide the convenience of using different computing options when available. It is also important to build numerical models that have regularity when the computing platform changes by using corresponding options of the numerical solver. The consistency between the Boeing and GWU platforms is shown in figures 36, 37, and 38 for the corresponding thicknesses of 1/16", 1/8", and 1/4", respectively. Mesh-III was chosen as the baseline model for this comparison and LLNL-3 material model parameters were employed for both analyses. It was observed that the correlation between Boeing and GWU computers were reasonably close when each model was used interchangeably and compared with enough confidence.

The other area of interest between the cross-platform studies is the computational cost. Normalized computational costs are compared in figure 39 for a better perception of the importance of selecting the right computing platform for ballistic impact analysis.



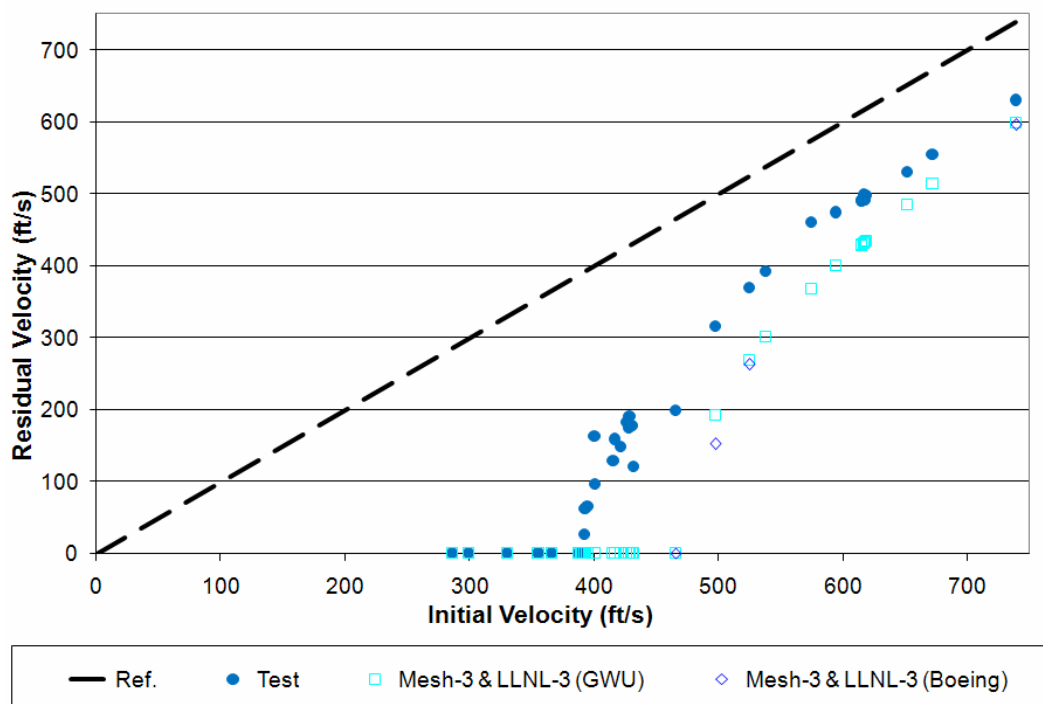


Figure 36. Platform Dependency for Target Thickness 1/16"

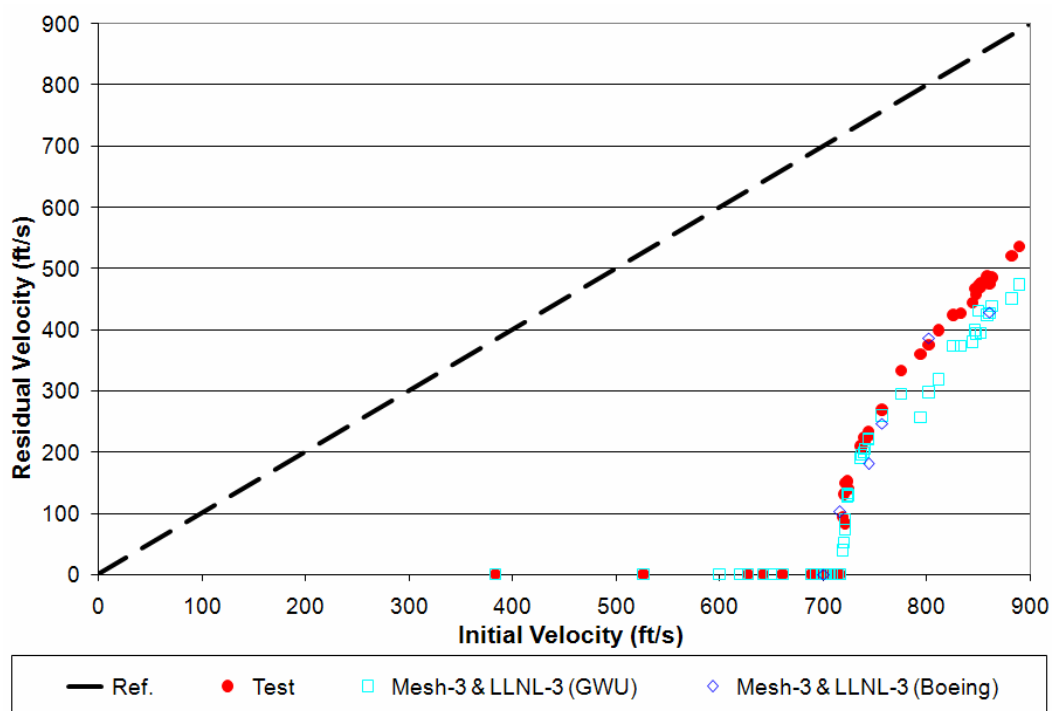


Figure 37. Platform Dependency for Target Thickness 1/8"

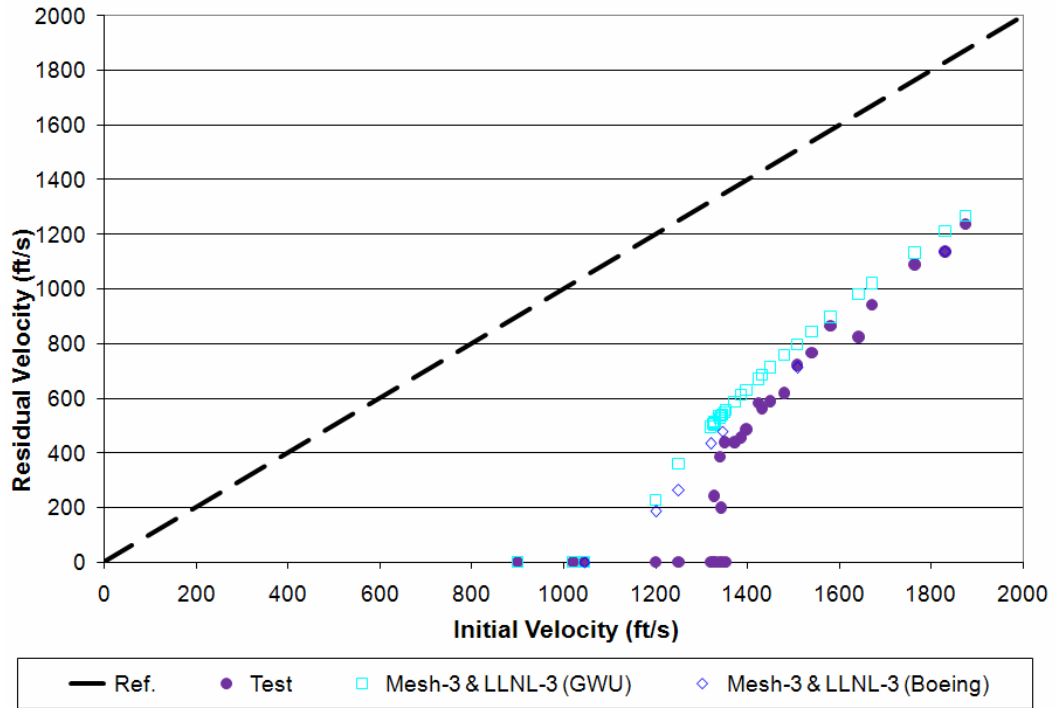


Figure 38. Platform Dependency for Target Thickness 1/4"

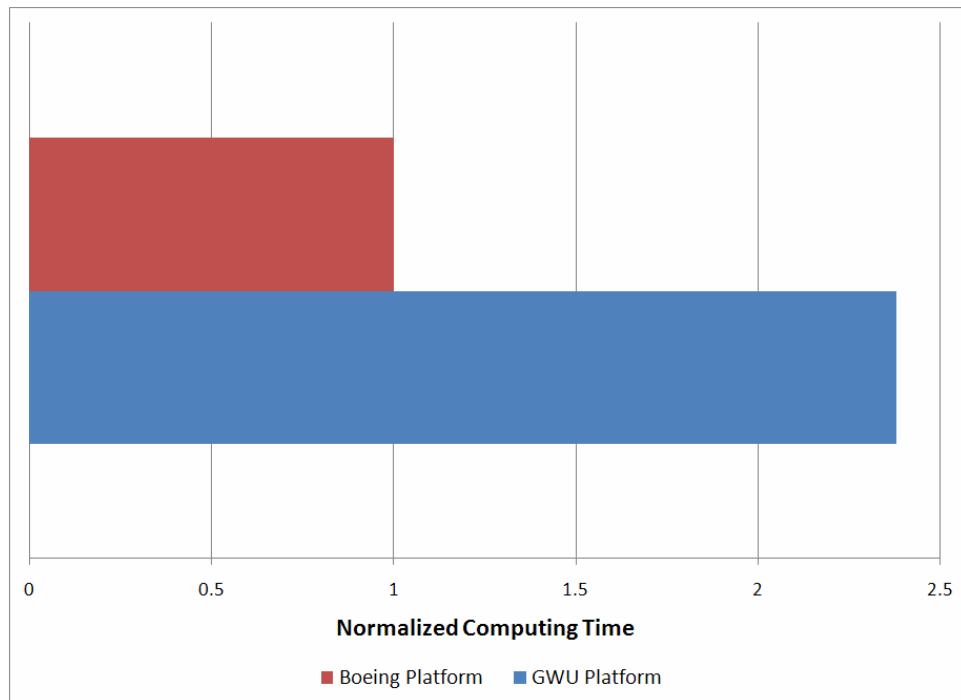


Figure 39. Cross-Platform Comparison of the Normalized Computing Costs

## 5.2 BALLISTIC LIMIT SUMMARY AND DISCUSSION.

Evaluation tasks accomplished within the framework of this effort included the assessment of four different material model parameters, while predicting the results of the ballistic impact tests conducted by UCB.

Experimental findings with the simulation results that were obtained for different sets of material model parameters are compared in figures 29, 32, and 35. The predictive performance of the simulations for 1/16" material was found to be promising for all parameters except the LLNL-3 set; this was expected since this particular set was tuned for the thicker targets. However, as the material thickness increased, the accuracy (when compared to experimental results) decreased. A single set of material model parameters is not able to keep the same predictive capability during the simulation of various thicknesses because as the thickness changes, (also with the increase in ballistic limit), the type of deformation and failure changes drastically from petaling to plugging, as shown in figure 40. Bending and necking deformation patterns change to shearing and spalling deformations.

Material model parameters are usually calibrated for a particular material gauge length and are not adjusted or tuned dynamically according to the changes and transitions in deformation and failure. Therefore, some compromise in the predictive performance during transitions was expected. The results from sections 4.1, 4.2, and 4.3 also show that in-plane or through-the-thickness mesh sensitivities also depend on the material model parameters.

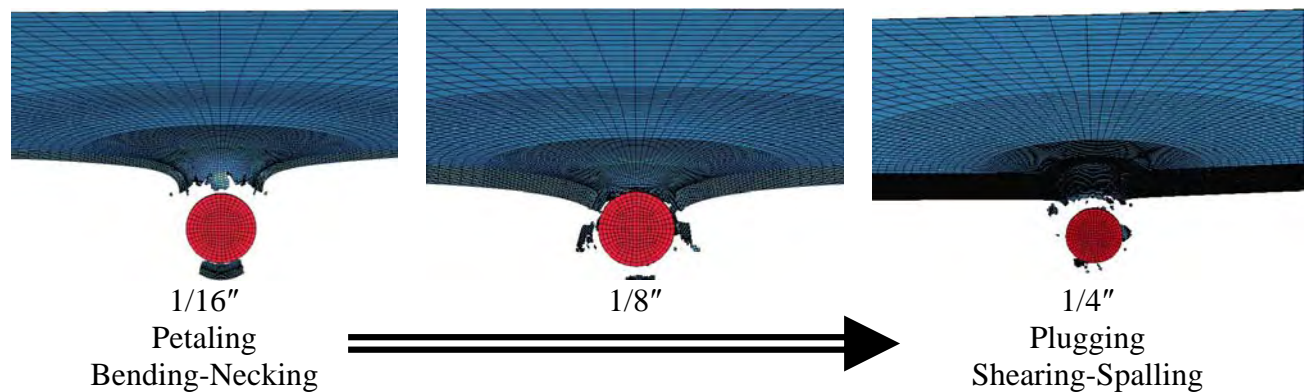


Figure 40. Transition of the Failure Mode

The preferred contact definition chosen for this study was \*CONTACT\_ERODING\_SINGLE\_SURFACE with SOFT=1 and the defaults for the rest of the input. The segment-based contact, SOFT=2 seemed to be equally accurate, but is much more costly in CPU time.

The \*MAT\_NONLOCAL smoothing option in LS-DYNA did not improve the accuracy nor decrease the mesh dependency. However, it has features that warrant further work in this respect with a compromise in the computational cost.

## 6. COMPARING AND DISCUSSING THE PENETRATION EQUATIONS.

The FAA and Naval Air Warfare Center Weapons Division in China Lake, CA have developed an aircraft-level vulnerability analysis to study uncontained engine failure hazards [12]. This analysis uses an empirically derived penetration equation known as the “FAA penetration equation.” In this equation, the ballistic limit and the residual velocity are expressed as a function of the projectile mass, velocity, projected area, projected perimeter, target thickness, and dynamic shear modulus. It should be noted that the projectile shape and size are embedded into the projected area, perimeter, and mass.

To gain insight into the assumption about the validity of the projected area, the cylindrical and cubical projectile penetrations were computed with LS-DYNA. No test data is available for these cases, but these runs are informative when compared with the results from the sphere tests. The cube and cylinder projectiles have the same mass and the same projected area as the sphere; similarly, the computations were done with the same Al plates as those used with the sphere. The plate mesh pattern with the cylinder was circular, as was the plate mesh pattern for the sphere, since the failure zone was circular. However, the mesh pattern with the cube projectile was square, because the failure zone under the impact from the cube was square. (The FE meshes are shown in figures 7 and 8.) The results of the simulations with cylindrical and cubical projectiles were compared with the equivalent spherical projectile responses, while Mesh-I was used with LLNL-3 J-C material model set. The results of this comparison are shown in figures 41, 42, and 43 for the corresponding thicknesses of 1/16", 1/8", and 1/4", respectively. Clearly, the figures show that the results do not match well.

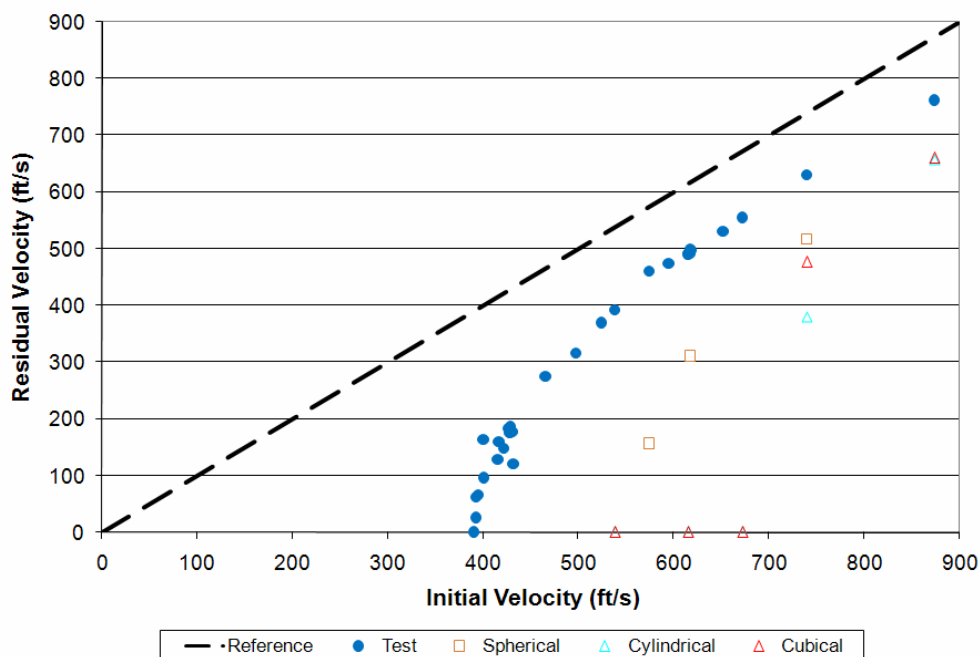


Figure 41. Ballistic Limit Comparison for Spherical, Cubical, and Cylindrical Projectiles for 1/16" Target

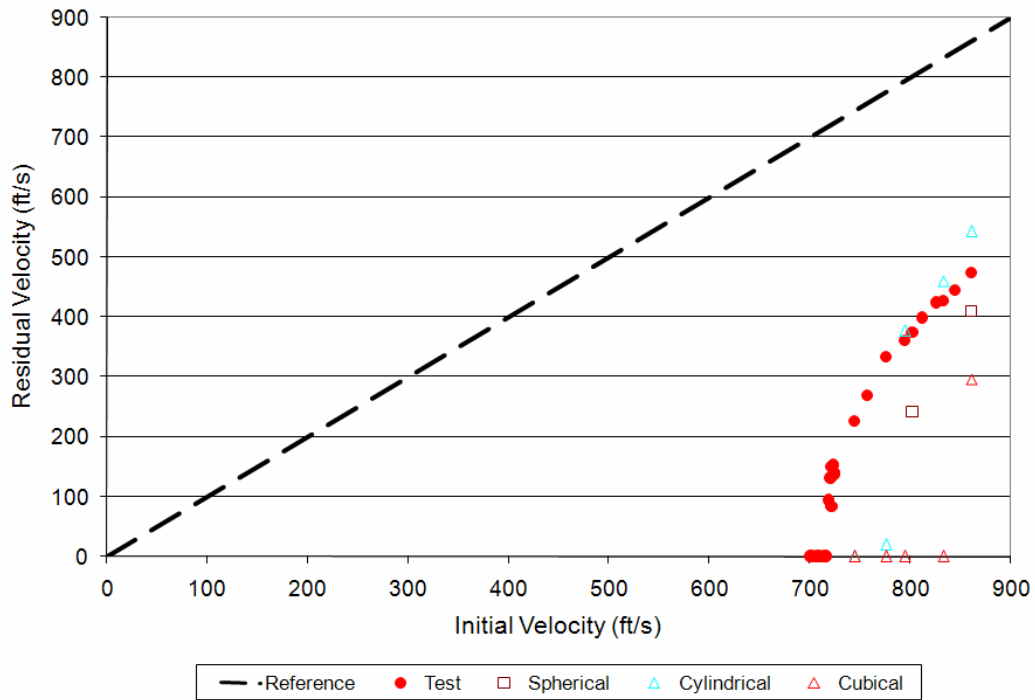


Figure 42. Ballistic Limit Comparison for Spherical, Cubical, and Cylindrical Projectiles for 1/8" Target

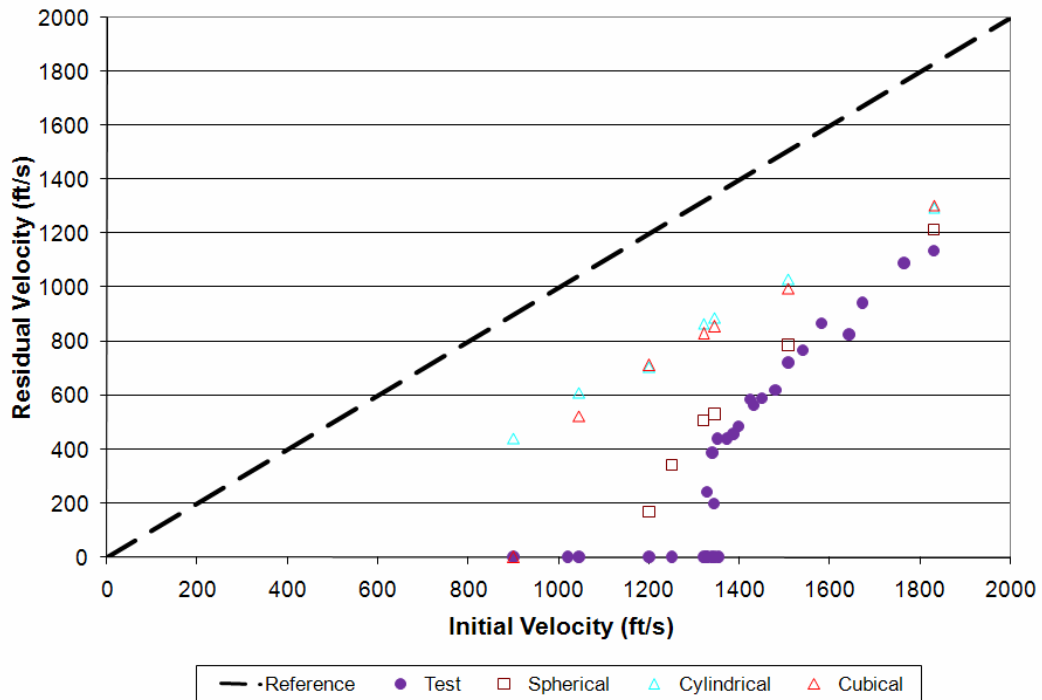


Figure 43. Ballistic Limit Comparison for Spherical, Cubical, and Cylindrical Projectiles for 1/8" Target

The ballistic limit in this work is defined as the limit velocity when the projectile is stopped without any exit velocity and a small increase in the velocity would then give a nonzero exit velocity [13].

The ballistic limits for the three thicknesses were determined using (1) the UCB tests, (2) the LS-DYNA computations, and (3) the FAA penetration equations. The FAA penetration equations are discussed in detail, for example, in reference 12. The results are shown in figure 44.

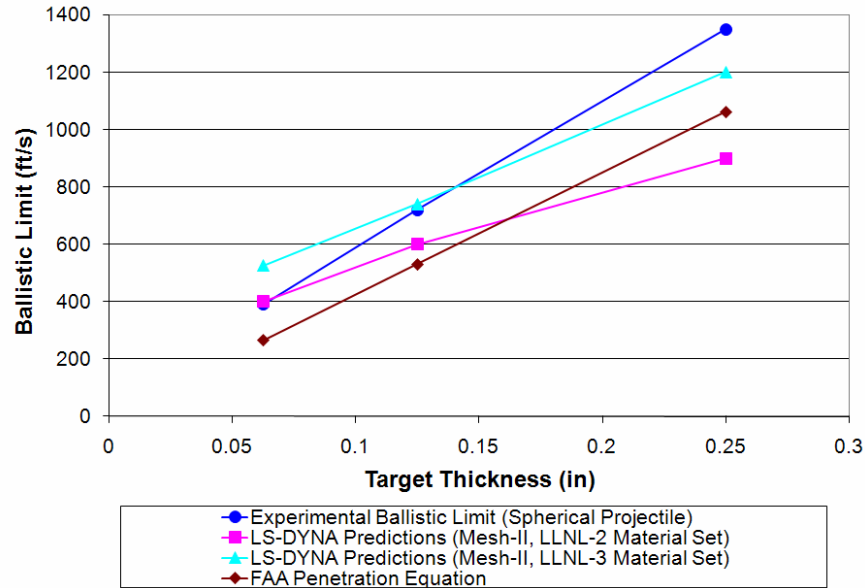


Figure 44. Comparison of the Ballistic Limit Predictions

The FAA equation makes the assumption that penetration is related to the projectile shape in a way that the projectile is completely defined by the projected area, perimeter, and its mass. The equation uses an empirically defined constant that was developed by performing a significant test series using real blade fragments against aircraft fuselage structure. It was not tuned for spherical impactors, which create more deformation and result in higher ballistic limit ( $V_{50}$ ) values. In practice, users should test their proprietary materials to define the needed coefficients for each of these analyses. The latest version of the Uncontained Engine Debris Damage Analysis Model (UEDDAM) includes a series of user-defined material constants for the FAA penetration equation specifically for this purpose. For the summary shown in figure 44, the LS-DYNA results were selected from the Mesh-II simulations outlined in section 3.1. The most accurate cases were selected. LLNL-2 material data gives the best results for thin plates, because it was developed based on thin plate test data. LLNL-3 material data gives the best results overall since it used all of the data and minimized the errors across the thickness range, which resulted in overpredicting the  $V_{50}$  for thin material and underpredicting the  $V_{50}$  for thick material, as illustrated in figure 44. The FAA equation curve is similar to the actual test curve but has a lower ballistic limit. This may be due to the fact that the FAA penetration equations were derived from ballistic penetration tests in which actual blade fragments were shot at commercial aircraft fuselage skin structure instead of ideal spherical projectiles.

## 7. CONCLUSIONS.

The University of California Berkeley ballistic tests were simulated by using LS-DYNA as an explicit dynamics finite element code incorporating Johnson-Cook (J-C) material model with four different sets of parameters. It was found that a single set of material model parameters may not necessarily predict the ballistic impact performance of a material accurately if significant change and transition occurs in the deformation mode. The simulation results showed that the effect of the change in thickness from thinner to thicker targets caused the change in the deformation type and failure from petaling to plugging, respectively.

It was found that the set of material model parameters that are tuned for a specific element size gave better accuracy. Otherwise, increasing the element density did not improve the performance significantly.

It is concluded that it is necessary to recalibrate the J-C damage parameters to attain a better consistency between simulations and the available ballistic limit measurements. However, transition of the failure mode makes it impossible to capture the change in deformation and failure by using a single set of parameters. The current material law does not allow adjusting the material model parameters dynamically. Therefore, it is also concluded that development of a new material law is necessary that can encounter the change and transition in the failure mode.

The soft-constraint (SOFT=1) and segment-based contact (SOFT=2) options in the contact definition, which use node-versus-segment and segment-versus-segment based force transfer algorithms, respectively, produced nearly identical results since almost identical mesh densities were used for both the target and projectile providing an uniform force distribution, where segment-based contact is found to be computationally more expensive.

The nonlocal failure criterion was exercised; however, in this limited study, there was no clear advantage from it despite the fact that it was computationally more costly. The topic warrants further research.

## 8. REFERENCES.

1. Johnson, G.R. and Cook, W.H., "A Constitutive Model and Data for Metals Subject to Large Strains, High Strain Rates and High Temperatures," *Seventh International Symposium on Ballistics*, The Hague, The Netherlands, April 1983.
2. Lesuer, D.R., "Experimental Investigations of Material Models for Ti-6Al-4V Titanium and 2024-T3 Aluminum," FAA report DOT/FAA/AR-00/25, September 2000.
3. Kay, G., "Failure Modeling of Titanium 6Al-4V and Aluminum 2024-T3 With the Johnson-Cook Material Model," FAA report DOT/FAA/AR-03/57, September 2003.
4. Kay, G., Goto, D., and Couch, R., "Statistical Testing of Aluminum, Titanium, Lexan and Composites for Transport Airplane Rotor Burst Fragment Shielding," FAA report DOT/FAA/AR-07/26, August 2007.

5. Kelly, S. and Johnson, G., "Statistical Testing of Aircraft Materials for Transport Airplane Rotor Burst Fragment Shielding," FAA report DOT/FAA/AR-06/9, May 2006.
6. Gogolowski, R.P. and Morgan, B.R., "Ballistic Experiments With Titanium and Aluminum Targets," FAA report DOT/FAA/AR-01/21, April 2001.
7. Loikkanen, M.J., Buyuk, M., Kan, C.D., and Meng, N., "A Computational and Experimental Analysis of Ballistic Impact to Sheet Metal Aircraft Structures," 5<sup>th</sup> *European LS-DYNA Users Conference*, Birmingham, UK, May 25-26, 2005.
8. Zukas, J.A., *High Velocity Impact Dynamics*, John Wiley, New York, 1990.
9. Kurtaran, H., Buyuk, M., and Eskandarian, A., "Design Automation of a Laminated Armor for Best Impact Performance Using Approximate Optimization Method," *International Journal of Impact Engineering*, Vol. 29, 2003, pp. 397-406.
10. Kurtaran, H., Buyuk, M., and Eskandarian, A., "Ballistic Impact Simulation of GT Model Vehicle Door Using Finite Element Method," *Theoretical and Applied Fracture Mechanics*, Vol. 40, 2003, pp. 113-121.
11. Hallquist, J.O., "LS-DYNA Keyword User's Manuel," Livermore Software Technology Corporation, Livermore, CA, USA, 2003.
12. Lundin, S.J. and Mueller, R., "Advanced Aircraft Materials, Engine Debris Penetration Testing," FAA report DOT/FAA/AR-03/37, December 2005.
13. Goldsmith, W., "Review: Non-Ideal Projectile Impact on Targets," *International Journal of Impact Engineering*, Vol. 22, 1999, pp. 95-395.